International Journal of Heat and Fluid Flow 112 (2025) 109705

Contents lists available at ScienceDirect

International Journal of Heat and Fluid Flow

journal homepage: www.elsevier.com/locate/ijhff

Unsteady Reynolds-Averaged Navier-Stokes simulation of turbulent flow fields around a line of trees and a steep hill using a new turbulent inflow generation method

Takeshi Ishihara, Xiangyan Chen *

Department of Civil Engineering, School of Engineering, The University of Tokyo, Tokyo, Japan

ARTICLE INFO

Keywords:
A new turbulent inflow generation method
Turbulent flow field
Line of trees
Steep hill
Unsteady Reynolds-Averaged Navier-Stokes

ABSTRACT

In this study, mean and turbulent flow fields around a line of trees and a steep hill are investigated by unsteady Reynolds-Averaged Navier-Stokes (URANS) simulation with a new turbulent inflow generation method. First, an inflow generation method is presented for the URANS model, utilizing a prespecified averaging time to divide the turbulent flow fields into resolved and modelled parts and ensure conservation of the total turbulence kinetic energy. The turbulent flow fields reproduced by the URANS model are then evaluated over flat terrain, a line of trees and a steep hill to demonstrate the performance of the URANS model. A large averaging time can be applied to the URANS model for flat terrain and a line of trees because the turbulent flow field can be simulated well by the turbulence model, but suitable averaging times are required for the URANS simulation to predict large separation vortices behind the steep hill as resolved coherent structures. Finally, an indicator is proposed to assess the performance of turbulence models considering the prediction accuracy and computational efficiency. The proposed method exhibits the best performance in predicting the mean velocity and turbulence kinetic energy, compared to Reynolds-Averaged Navier-Stokes model and Large Eddy Simulation.

1. Introduction

Turbulent flow is essential for wind conditions at pedestrian level around buildings (Blocken and Carmeliet, 2008; Tsang et al., 2012; Janssen et al., 2013), neutral ventilation of buildings (Kobayashi et al., 2009; Karava and Stathopoulos, 2012; van Hooff and Blocken, 2013), wind-driven rain (Blocken and Carmeliet, 2006; Blocken et al., 2010; Kubilay et al., 2013), wind resource assessment over urban areas and complex terrains (Watanabe and Uchida, 2015; Ishihara and Qi, 2019; Qian and Ishihara, 2019; Ishihara et al., 2020; Chen et al., 2020) and structure safety analysis (Zhang et al., 2021; Wang et al., 2022). In these engineering applications, accurate simulations of both mean and turbulent flow fields are crucial. At the same time, more than 12 wind directions are required to account for the impact of complex terrains on the mean and turbulent flow fields (Yamaguchi et al., 2003; Ishihara et al., 2020), leading to high computational cost. Currently, Reynolds-Averaged Navier-Stokes (RANS) and Large Eddy Simulation (LES) are widely used for predictions of flow fields in urban areas and over complex terrain. However, these two approaches cannot satisfy the requirements for high prediction accuracy and low computational cost at the same time, since the prediction accuracy and computational cost are in a trade-off relationship.

The first approach is RANS. Undoubtedly, RANS is a widely used turbulence model in engineering applications owing to its low computational cost, as only steady-state solutions are considered in the simulation. Regarding prediction accuracy, Ferreira et al. (1995) conducted numerical simulations of two-dimensional rough ridges and found that the drag coefficients were well simulated. Ishihara and Hibi (2002) simulated the wind field around a three-dimensional rough hill by standard k-ε model and Shih's non-linear k-ε model. The results showed that Shih's non-linear k-ε model matched better with the experiment than the standard k-ε model. However, Balogh et al. (2012) applied the newly proposed k-ε model to a three-dimensional smooth hill, the predicted turbulence kinetic energy deviated significantly from the experiment. The reason why the conventional RANS cannot provide accurate results is that it fails to simulate organized motions generated by obstacles such as buildings and steep hills (Tominaga, 2015; Qi and Ishihara, 2018). In conclusion, RANS has low computational cost but is inaccurate, especially for turbulent flow fields with coherent structures such as complex terrain and urban areas.

* Corresponding author.
E-mail addresses: ishihara@bridge.t.u-tokyo.ac.jp (T. Ishihara), x.chen@bridge.t.u-tokyo.ac.jp (X. Chen).

https://doi.org/10.1016/j.ijheatfluidflow.2024.109705
Received 29 July 2024; Received in revised form 6 October 2024; Accepted 3 December 2024

The second approach is LES, which is used to reproduce turbulent flow fields over complex terrains and in urban areas (Iizuka and Kondo, 2004; Ren et al., 2018; Qi and Ishihara, 2018; Qian and Ishihara, 2019; Ishihara et al., 2020; Yang et al., 2020; Yang et al., 2021; Zhou et al., 2022). LES has shown good prediction accuracy for turbulent flow fields because it can reproduce organized structures in the wake region of obstacles. However, as pointed out by Qian and Ishihara (2019), very fine grids are essential to resolve near-wall turbulence in LES, which makes the numerical simulation very time-consuming. Furthermore, Béghein et al. (2010) summarized that not only does the numerical grid scale need to be one or two orders of magnitude larger than the Kolmogorov microscale, but also the timestep size should be sufficiently small because turbulence is inherently unsteady. As an extension of LES, the accuracy of detached-eddy simulation (DES) and delayed detached-eddy simulation (DDES) also depends on the grid resolution and time-step size. Overall, LES is accurate for predicting both mean and turbulent flow fields, assuming a sufficiently small grid and timestep, but it can be very time-consuming to predict the wind fields even over flat or gently undulating terrain.

Compared with RANS, URANS can be employed to predict flows with periodic motions caused by large-scale organized structures in engineering applications. Therefore, URANS is considered as a bridge strategy that combines the advantages of RANS with those of LES (Girimaji, 2006) in terms of prediction accuracy and computational efficiency. In the field of civil engineering, Kato and Launder (1993), Shimada and Ishihara (2002), Younis and Przulj (2006) applied URANS to rectangular cylinders with different aspect ratios and favorably predicted the vortex shedding and vibration of the rectangular cylinders. The inflow in these simulations is uniform because the turbulence intensity is very low for long-span bridges over oceans and rivers. In the field of mechanical engineering, Mikuz and Tiselj (2017), Baglietto et al. (2017), Xu (2020), Feng et al. (2021) validated the efficiency and accuracy of the URANS model, i.e., k-ω SST and STRUCT-ε models, for prediction of the flow fields around rod bundle, T-junction, freight train, Ahmed body, DrivAer model, periodic hills and asymmetric diffusers. In these cases, the inflow is assumed to be smooth. However, one of the limitations of URANS pointed out by Ishihara and Qi (2019) is that in the turbulent boundary layer, if steady inflow adopted in URANS is the same as that in RANS, the turbulent flow field in the wake region predicted by URANS is almost the same as that predicted by the RANS model. Therefore, a method of generating the turbulent inflow is crucial to make the most of URANS's ability to reproduce turbulent flow fields.

To evaluate new turbulence models, Lenci (2016) introduced five criteria: low computational cost, potential accuracy, flow description, robustness, and ease of use. Among these, flow description is adopted to visualize the flow field but is not used to evaluate the statistical behavior of the flow field and cannot be calculated quantitatively. Robustness is primarily concerned with the numerical stability of the turbulence model, while ease of use aims to evaluate the usability of the turbulence model. In engineering applications, potential accuracy and computational cost are the most important considerations. Therefore, this study focuses only on the criteria of prediction accuracy and computational efficiency and proposes an indicator to evaluate the performances of both together.

This study aims to (1) propose a new inflow generation method that separates the turbulence into a resolved part and a modelled part for unsteady Reynolds-Averaged Navier-Stokes (URANS) model, (2) provide a method to impart the larger low frequency turbulent structures at the inflow, while modelling the smaller scale turbulence using a two-equation eddy viscosity model modified to accommodate the interactions between large and small structures, (3) simultaneously achieve prediction accuracy and computational efficiency using URANS with the new inflow generation method and demonstrate its performance in predicting turbulent flows over flat terrain, tree lined areas and steep hills. The proposed method bridges the gap between RANS and LES in terms of prediction accuracy and computational efficiency, and also improves the performance of the traditional URANS, making it applicable to a wide range of engineering applications, such as prediction of dynamic wakes of obstacles and vortex-induced vibrations of structures in turbulent inflows, etc., which cannot be reproduced by RANS. The computational time of URANS using the new inflow generation method is much shorter than that of LES because it is insensitive to the time step size and the conservation of total kinetic energy is satisfied during the simulation. In Section 2, numerical models are described, including governing equations and numerical scheme, the prespecified averaging time and turbulent inflow used in URANS, and indicators for evaluating the performance of turbulence models. Section 3 presents the validation of turbulent flow fields predicted by the URANS model over flat terrain, a line of trees and a steep hill. Section 4 discusses the prediction accuracy and computational cost, and evaluates the performance of RANS, LES and URANS using three turbulent flow fields. Finally, Section 5 summarizes the conclusions in this study.

2. Numerical models

The governing equations and numerical scheme for the three typical turbulence models are presented in Section 2.1. In Section 2.2, the grid systems for numerical simulations are introduced for the cases of a line of trees and a steep hill. The prespecified averaging time and turbulent inflow generation methods for the URANS model is clarified in Section 2.3. Section 2.4 presents several indicators to evaluate the performance of turbulence models.

2.1. Governing equations and numerical scheme

As demonstrated by Rodi (1993) and Tominaga (2015), the instantaneous velocity fluctuations caused by coherent structures in turbulent flow fields are illustrated in Fig. 1 and expressed as,

$$u_i(t) = \widetilde{u}_i(t) + u_i'(t),\ \overline{u}_i = \overline{\widetilde{u}}_i \tag{1}$$

where $u_i(t)$ is the time series of instantaneous velocity in the i th direction. $\widetilde{u}_i(t)$ is the time series of grid or ensemble averaged velocity. $u_i'(t)$ is the time series of stochastic turbulent fluctuations. For RANS, Reynolds averaging process is conducted and the mean velocity $\overline{u_i}$ is predicted by steady simulations. For LES, all the velocity components are resolved explicitly based on grid resolution (Luis, 2012) and the mean velocity $\overline{u_i}$ is calculated from the grid averaged velocity $\overline{\widetilde{u}}_i$. For URANS, the ensemble averaged velocity is resolved by transient simulations and the mean velocity $\overline{u}_i$ is calculated from the ensemble averaged velocity $\overline{\widetilde{u}}_i$, while the stochastic turbulent fluctuation is predicted

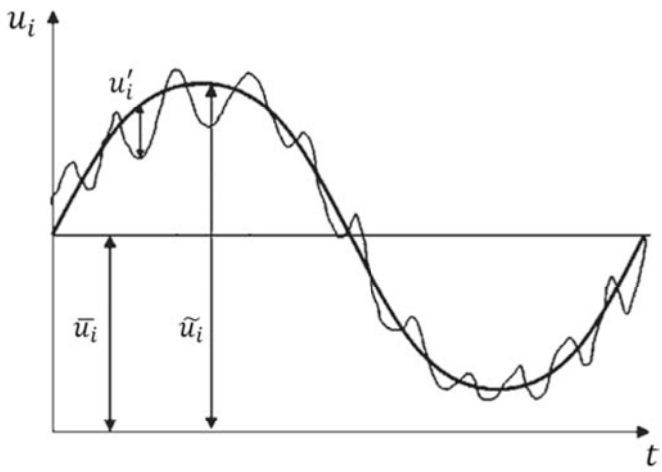

Fig. 1. Velocity fluctuations due to coherent structures (Rodi, 1993; Tominaga, 2015).

by transport equations. Although the mean velocity for both LES and URANS is expressed similarly, the ensemble averaged velocity and the stochastic turbulent fluctuation is separated by grid in LES and by time in URANS.

In incompressible flows, the governing equations of continuity and momentum are averaged over the computational grids or the averaging time and are written as,

$$\frac{\partial\left(\rho\widetilde{u}_i\right)}{\partial x_i}=0 \tag{2}$$

$$\rho\frac{\partial\widetilde{u}_i}{\partial t}+\rho\frac{\partial\left(\widetilde{u}_j\widetilde{u}_i\right)}{\partial x_j}=-\frac{\partial\widetilde{p}}{\partial x_i}+\frac{\partial}{\partial x_j}\left[\mu\left(\frac{\partial\widetilde{u}_i}{\partial x_j}+\frac{\partial\widetilde{u}_j}{\partial x_i}\right)\right]+\frac{\partial\tau_{ij}}{\partial x_j}+f_{\widetilde{u},i} \tag{3}$$

where $\widetilde{p}$ is the resolved pressure. ρ is the air density and μ presents the molecular viscosity. $f_{\widetilde{u},i}$ denotes the fluid force. For RANS, on the left side of Eq. (3), the first term equals zero. The stress τ_{ij} is usually modelled by eddy-viscosity hypothesis and is expressed as,

$$\tau_{ij}=2\mu_t\widetilde{S}_{ij}+\frac{\delta_{ij}}{3}\tau_{kk} \tag{4}$$

$$\widetilde{S}_{ij}=\frac{1}{2}\left(\frac{\partial\widetilde{u}_i}{\partial x_j}+\frac{\partial\widetilde{u}_j}{\partial x_i}\right) \tag{5}$$

where μ_t is the turbulence viscosity. δ_{ij} is the Kronecker delta function. $\widetilde{S}_{ij}$ is the strain rate tensor and is calculated in Eq. (5).

As mentioned by Spalart (2000) and Hart (2016), there are two primary model categories: Reynolds-Averaged Navier-Stokes, such as RANS, URANS, and Scale-Resolving Simulation, such as LES, DES, DDES. The turbulence viscosity is related to turbulence models. Fig. 2 presents the turbulence kinetic energy among LES, URANS and RANS models as shown in a turbulence spectrum. f_{ap} denotes the frequency according to averaging period for a target wind speed, f_{pf} represents the peak frequency of the spectrum, and f_{ny} is the Nyquist frequency, which is half the sampling frequency.

For RANS, all the turbulence kinetic energy k between f_{ap} and f_{ny} as shown in Fig. 2 is modelled and predicted directly. Regarding LES, the turbulence kinetic energy $\widetilde{k}$ between f_{ap} and f_{ave} is resolved, while the high frequency turbulence between f_{ave} and f_{ny} is modelled with a sub-grid scale model due to grid resolution limitations (Luis, 2012). In the case of URANS, f_{ave} represents the boundary of resolved and modelled turbulence and coincides with the prespecified time of turbulent inflow generation method introduced in Sect. 2.2.

According to the three turbulence models, the instantaneous and mean turbulence kinetic energy are expressed as follows:

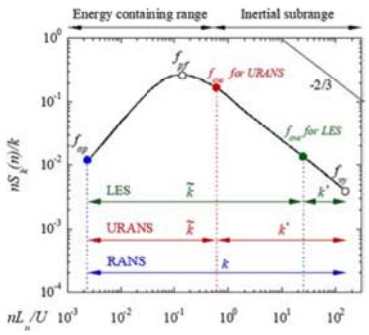

Fig. 2. Schematics of averaging time in LES and URANS through spectrum.

$$k(t)=\widetilde{k}(t)+k'(t) \tag{6}$$

$$\overline{k}=\overline{\widetilde{k}}+\overline{k'} \tag{7}$$

where $k(t)$ is the time series of total turbulence kinetic energy. $\widetilde{k}(t)$ represents the time series of the resolved turbulence kinetic energy in LES and URANS. $k'(t)$ is the time series of modelled turbulence kinetic energy. $\overline{k'}$ is the mean value of the modelled turbulence kinetic energy in LES, which is neglected in this study since most of the turbulence in LES is resolved. k' in URANS is calculated by a low-pass filter, which is predicted by a transport equation. In URANS, k' is called k_S to distinguish it from k' in RANS. For RANS, the total turbulence kinetic energy $\overline{k}$ equals to the modelled turbulence kinetic energy $\overline{k'}$.

The turbulence viscosity in LES is expressed as:

$$\mu_t=\rho L_S^2\sqrt{\widetilde{S}_{ij}\widetilde{S}_{ij}} \tag{8}$$

$$L_S=\min\left(\kappa d, C_S V^{\frac{1}{3}}\right) \tag{9}$$

where L_S is the mixing length for a sub-grid, the von Karman constant $\kappa=0.42$, C_S is the Smagorinsky constant and $C_S=0.032$ is adopted (Oka and Ishihara, 2009). d is the distance away from the nearest wall.

On the other hand, the turbulence viscosity in URANS is calculated as follows:

$$\mu_t=C_\mu\rho\frac{k_S^2}{\varepsilon_S} \tag{10}$$

where k_S and ε_S are the modelled turbulence kinetic energy and turbulence dissipation rate, which are computed from the transport equations by Xu, 2020 as follows:

$$\frac{\partial\rho k_S}{\partial t}+\frac{\partial\rho\widetilde{u}_j k_S}{\partial x_j}=\frac{\partial}{\partial x_j}\left[\left(\mu+\frac{\mu_t}{\sigma_k}\right)\frac{\partial k_S}{\partial x_j}\right]-\rho\widetilde{u_i u_j}\frac{\partial\widetilde{u}_j}{\partial x_i}-\rho\varepsilon_S \tag{11}$$

$$\begin{aligned}\frac{\partial\rho\varepsilon_S}{\partial t}+\frac{\partial\rho\widetilde{u}_j\varepsilon_S}{\partial x_j}&=\frac{\partial}{\partial x_j}\left[\left(\mu+\frac{\mu_t}{\sigma_\varepsilon}\right)\frac{\partial\varepsilon_S}{\partial x_j}\right]-C_{\varepsilon1}\rho\widetilde{u_i u_j}\frac{\partial\widetilde{u}_j}{\partial x_i}\frac{\varepsilon_S}{k_S}-C_{\varepsilon2}\frac{\rho\varepsilon_S^2}{k_S}\\&-\frac{C_\mu\rho\eta^3\left(1-\frac{\eta}{\eta_0}\right)}{1+\beta\eta^3}\frac{\varepsilon_S^2}{k_S}+S_\varepsilon\end{aligned} \tag{12}$$

where σ_k and σ_ε are the inverse effective Prandtl numbers for k_S and ε_S, respectively. The default constants are $C_\mu=0.0845$, $C_{\varepsilon1}=1.42$, $C_{\varepsilon2}=1.68$, $\sigma_k=\sigma_\varepsilon=1.393$ (Fluent, 2021).

The turbulence model in URANS in this study is the STRUCT-ε model by Xu, 2020. Compared to the standard k-ε model, two terms are added to the right-hand side of Eq. (12). The fourth term is from the conventional RNG k-ε model by Yakhot et al. (1992) and is used to describe the effects of rapid strain and streamline curvature, in which $\eta_0=4.38$, $\beta=0.012$. $\eta\equiv\left|\widetilde{S}\right|k_S/\varepsilon_S$ and $\left|\widetilde{S}\right|=\sqrt{\widetilde{S}_{ij}\widetilde{S}_{ij}}$.

The fifth term S_ε is the product of the constant $C_{\varepsilon3}$, the turbulence kinetic energy k_S and the second invariant of the resolved velocity gradient tension $\widetilde{II}$ and is used to describe the regions lack applicability of the scale-separation assumption as follows:

$$S_\varepsilon=C_{\varepsilon3}k_S\widetilde{II}=-\frac{C_{\varepsilon3}k_S}{2}\frac{\partial\widetilde{u}_i}{\partial x_j}\frac{\partial\widetilde{u}_j}{\partial x_i} \tag{13}$$

where the constant $C_{\varepsilon3}$ of 1.5 is determined by a sensitivity study by Xu, 2020.

For RANS, the modelled turbulence kinetic energy k_S, modelled turbulence dissipation rate ε_S and ensemble averaged velocity $\widetilde{u}_i$ in Eqs. (11) and (12) are replaced by the total turbulence kinetic energy $\overline{k}$, total

turbulence dissipation rate $\overline{\varepsilon}$ and mean velocity $\overline{u_i}$. The unsteady terms in the two equations are zero.

The boundary conditions and numerical scheme adopted in this study are described below. Symmetry conditions are applied to the side and top boundaries. The outlet boundary condition is pressure outlet. The bottom surface, including the steep hill, is defined as a non-slip wall with the surface roughness of $z_0 = 0.01$ mm as shown in Ishihara et al. (1999). The numerical simulations are conducted using ANSYS Fluent 16.2. The spatial discretization method is second order upwind for RANS and URANS, while the central differencing scheme is adopted for LES, as recommended by Yang (2015). The time discretization method for LES and URANS is the second order implicit scheme. The pressure–velocity coupling for the three turbulence models is Semi-Implicit Pressure Linked Equations (SIMPLE).

2.2. Grid system for numerical simulations

For the tree row, the schematic diagram can be found in Qi and Ishihara (2018). Fig. 3a presents a bird's eye view of the computational domain. The domain is 70 $H(x) \times 21\ H(y) \times 25\ H(z)$, where $H = 0.07$ m denotes the height of the trees. The inlet boundary is located $10H$ upstream the line of trees. A space of 60 H is allocated downstream to allow for vortex shedding behind the tree row. Fig. 3b illustrates a top view of the grid system and the specific locations P_0 through P_5 are highlighted. These locations are the subject of later discussion. Fig. 3c and Fig. 3d show a top view of the target zone and a close-up view of the tree row. Near the edge of the trees, grid refinement is performed with a mesh ratio of 1.15 and minimal grid resolution of 3 mm to accurately capture the flow separation. In the wake downstream the line of trees, a uniform grid of size 30 mm is used. Grid independence is verified by refining the grid to twice the initial resolution.

For the case of a steep hill with smooth surface, data from the wind tunnel experiment by Ishihara et al. (1999) are adopted for validation in this study. The shape of the steep hill is expressed as follows:

$$z_s(x,y) = \begin{cases} h\cos^2\left(\dfrac{\pi\sqrt{x^2+y^2}}{2L}\right), \sqrt{x^2+y^2} < L \\ 0, \sqrt{x^2+y^2} \geq L \end{cases} \tag{14}$$

where x, y and z are the longitudinal, lateral and vertical coordinates, respectively. The hill height is $h = 40$ mm and the hill radius is $L = 100$ mm. It is centered at $x = 0$ and $y = 0$. The second vertical coordinate $z' = z - z_s(x,y)$ represents the height above the ground. The cross section of the steep hill according to Eq. (14) is illustrated in Fig. 4.

Fig. 5a shows a bird's eye view of the computational domain of a steep hill. If the three-dimensional steep hill is taken out from the computational domain, it becomes the case of flat terrain hereafter. The domain is 90 $h(x) \times 16.5\ h(y) \times 22.5\ h(z)$, and the inlet boundary located 30 h upstream from the hill center. The downstream space is 60 h for the evolution of vortex shedding downstream the hill. Fig. 5b is the grid system of the entire computational domain where the inlet, P_1, P_2 and P_3 are plotted. Fig. 5c shows the target zone and Fig. 5d depicts the steep hill. The dotted lines in Fig. 5 indicate the boundary of the steep hill. In this study, 1.0 mm grid is adopted in the target region. A hybrid grid system similar to that employed by Ishihara and Qi (2019) is adopted to control the grid amount and improve computational efficiency. In Fig. 5b, the red rectangle containing the steep hill is the target zone with gird size of 1.0 mm. The elongated yellow rectangles upstream, downstream, above and below the target zone are buffer zones where triangular grids are used to gradually transition from fine grids to coarse grids. Upstream of the target zone, the grid size is 10 mm, while the grid size above and below the target zone is 8 mm.

2.3. Prespecified averaging time and turbulent inflow generation for URANS

As pointed out by Tominaga (2015) and Ishihara and Qi (2019), the potential of URANS to resolve periodic fluctuations will be limited if mean velocity and total turbulence kinetic energy are imported to the inlet boundary. Therefore, a prespecified averaging time should be used to separate instantaneous velocity into the resolved and modelled parts and applied to the inlet boundary. In the study, time-averaged Navier-Stokes simulation with a prespecified averaging time is referred to as URANS to distinguish it from the conventional unsteady Reynolds-averaged Navier-Stokes (URANS).

Turbulent inflow generation methods are generally classified into precursor and synthetic turbulence methods as shown by Zhou et al. (2022). As stated by Keating et al. (2004), the synthetic turbulence methods assume that turbulence can be characterized by low-order statistics. However, these methods often do not match the Reynolds-stress budget, and the perturbations decay quickly. In this study, the precursor method is adopted, where the perturbations are generated directly by the Navier-Stokes equations (Munters et al. 2016). In the precursor method, an auxiliary flow simulation, such as a large-eddy simulation on a flat plate, is performed. The exported flow field is

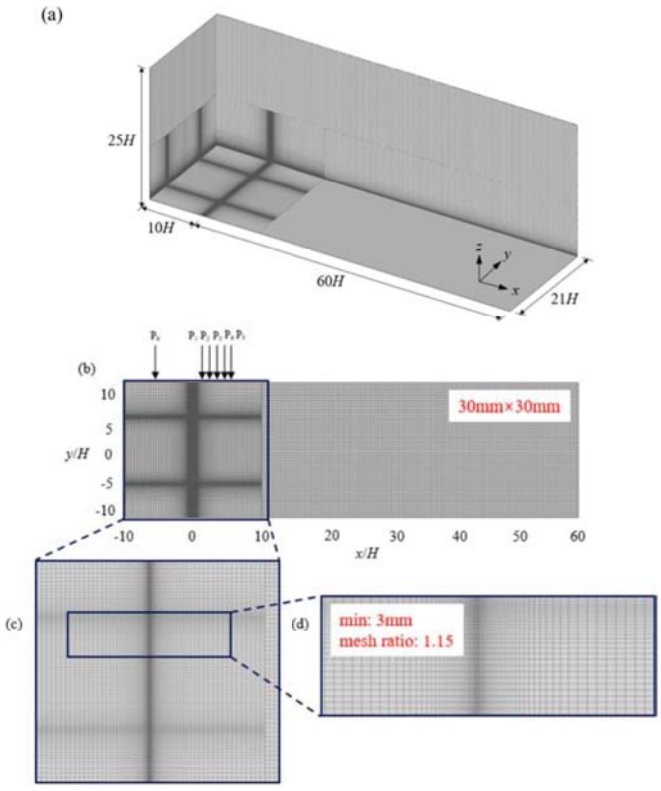

Fig. 3. Grid system and computational domain: a bird's eye view of the computational domain, b top views of entire area, c target zone and d a tree row.

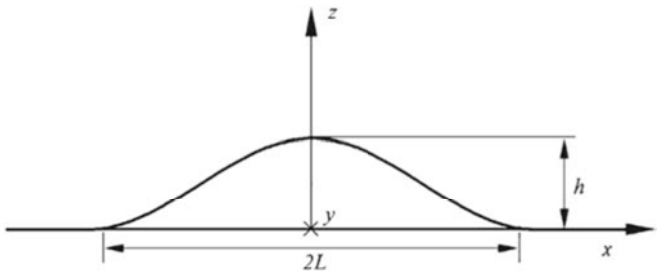

Fig. 4. Cross section of the steep hill.

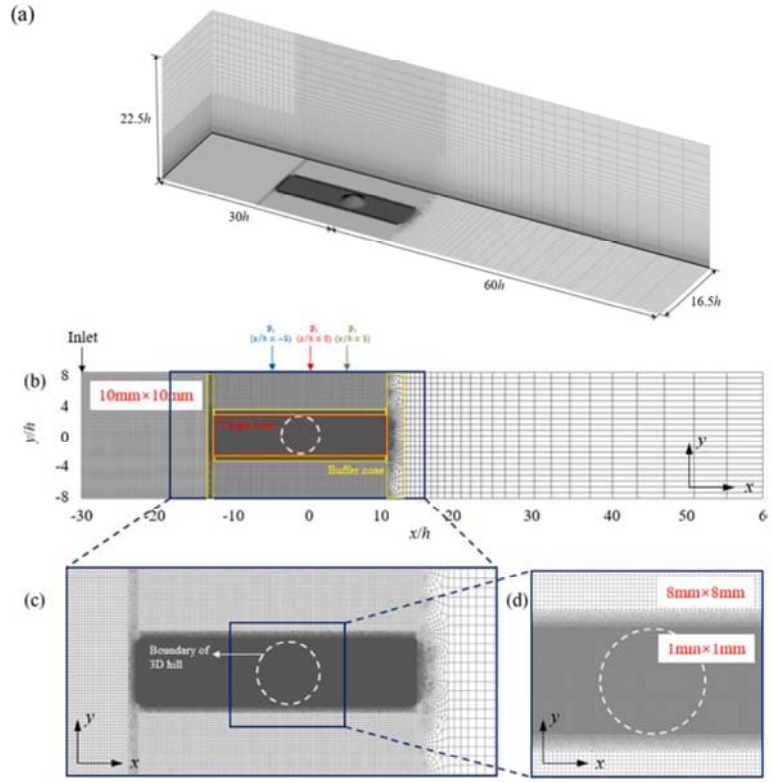

Fig. 5. Grid system and computational domain: a bird's eye view of the computational domain, b top views of entire area, c target zone and d a steep hill.

then smoothed based on a prespecified averaging time and imported to the inlet boundary. Fig. 6 shows the computational domains and the data export or import planes. The computational domain for the LES simulations and the data export plane are presented in Fig. 6b. The LES data in the export plane are stored in the database and reused in the URANS simulations as inflow data from the database as shown in Fig. 6a.

The computational time of URANS is much shorter than that of LES, since the database generated by LES can be reused. For example, in complex terrain or urban areas with the same upwind surface roughness subcategory, more than 12 wind directions are required to evaluate the wind resources or wind environments. This database can be used as the inflow for numerical wind tunnels and can also be used for different projects. The computational time of LES to generate the database of inflow is 8 h using an Intel Xeon CPU E5-2667 v4 with 88 cores and 960 GB memory, and this inflow database is then used repeatedly. The LES is run to statistical stationarity and LES simulation records long enough to capture this stationarity is saved for successively imparting to the inlet flow after filtering.

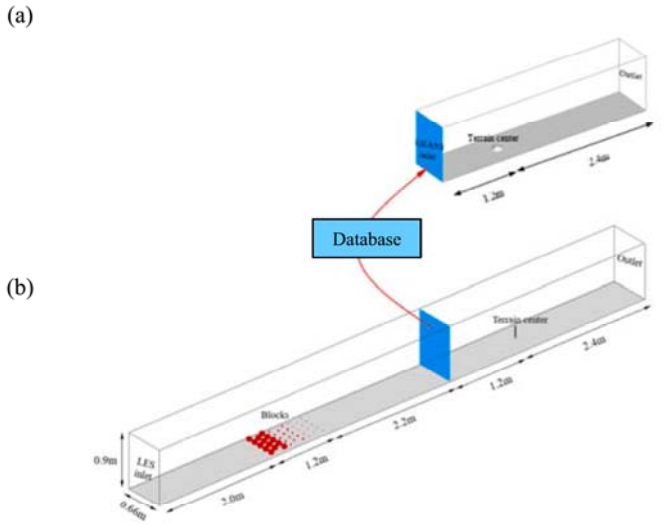

Fig. 6. Computational domains and data export or import planes: **a** computational domain for URANS and plane for data import; **b** computational domain for LES and plane for data export.

First, numerical simulations over flat terrain are carried out by LES to export the instantaneous velocity component $u_i(t) = [u_{i,1}, u_{i,2}, \cdots, u_{i,j}, \cdots, u_{i,n}]$, where i denotes the velocity component in the i direction, j is the j th data point and n is the total amount of data points. The time ratio γ_t is defined using the velocity spectrum as shown in Fig. 2 as follows:

$$\gamma_t = t_{ave}/T_p \tag{15}$$

where t_{ave} is the averaging time and T_p is the peak period and is equal to $1/f_{pf}$, here f_{pf} is the peak frequency as shown in Fig. 2. In this study, T_p is 30 s according to the wind tunnel experiment (Ishihara et al., 1999). The averaging time is the same as the time step of URANS simulation. Therefore, when the time ratio γ_t is larger than 1 $\gamma_t > 1$, the time step is larger than the peak period, which means that only large low-frequency vortices in energy containing rang are resolved and approaches to that by RANS if $\gamma_t \gg 1$, On the other hand, when the time ratio γ_t is smaller than 1, the time step in simulations is smaller than the peak period, which means that small high-frequency vortices in the inertial subrange are resolved and the flow field predicted by URANS is similar to that by LES. Prediction accuracy and computational efficiency can be achieved by appropriately determining γ_t.

Second, a low-pass filter is utilized to filter out the high-frequency fluctuating velocity component based on the prespecified averaging time and separate the turbulent flow field into the resolved and modelled parts. The low-pass filter used in this paper is the moving average with a sampling window d, which is related to the smoothness of the filtered velocity and determined as follows:

$$d = 2t_{ave}/\Delta t \tag{16}$$

where Δt is the time interval of the original dataset $u_i(t)$. The instantaneous resolved velocity $\widetilde{u}_{i,j}$, instantaneous modelled turbulence kinetic energy $k_{s,j}$ and dissipation rate $\varepsilon_{s,j}$ at the *jth* data point are calculated as follows:

$$\widetilde{u}_{i,j} = \frac{1}{d+1}\sum_{j-d/2}^{j+d/2} u_{ij} \tag{17}$$

$$k_{s,j} = \frac{1}{2}\sum_{i=1}^{3}\left(\frac{1}{d+1}\sum_{j-d/2}^{j+d/2}\left(u_{ij} - \widetilde{u}_{ij}\right)^2\right) \tag{18}$$

$$\varepsilon_{s,j} = \frac{C_\mu^{3/4} k_{s,j}^{3/2}}{\kappa z} \tag{19}$$

where $u_{i,j}$ and $\widetilde{u}_{i,j}$ are the instantaneous velocity and mean velocity in the i direction at the *jth* data point. After applying the moving average, the high-frequency fluctuation in the instantaneous velocity is filtered out by Eq. (17). The modelled turbulence kinetic energy $k_{s,j}$ can be calculated by the original velocity $u_{i,j}$ and the moving averaged velocity $\widetilde{u}_{i,j}$ by Eq. (18). Finally, the modelled turbulence dissipation rate, $\varepsilon_{s,j}$ is calculated by Eq. (19) using $k_{s,j}$.

Finally, the resolved velocity $\widetilde{u}_{i,j}$, modelled turbulence kinetic energy $k_{s,j}$ and dissipation rate $\varepsilon_{s,j}$ after the moving average are imported to the inlet grid. The dataset of resolved velocity, $\left[\widetilde{u}_{i,1}, \widetilde{u}_{i,2}, \cdots, \widetilde{u}_{i,j}, \cdots, \widetilde{u}_{i,m}\right]$, has a total number of data points $m = n\Delta t/t_{ave}$. The flowchart of three steps to generate turbulent inflow is illustrated in Fig. 7.

More information on RANS, LES and URANS can be found in Ishihara and Qi (2019). The difference between RANS, LES and URANS for the inflow used in this study is summarized in Table 1. For RANS, the mean velocity $\overline{u}_i$, the total turbulence kinetic energy $\overline{k}$ and the turbulence dissipation rate $\overline{\epsilon}$ are applied to the inlet boundary. For LES, the instantaneous velocity $u_i(t)$ are imported to the inlet boundary and the total turbulence kinetic energy is calculated using only the filtered velocity $\widetilde{u}_i(t)$. On the other hand, for URANS, not only the filtered velocity $\widetilde{u}_i(t)$ but also the modelled turbulence kinetic energy $k_S(t)$ and turbulence dissipation rate $\varepsilon_S(t)$ obtained from Eqs. (18) and (19) are imported to the inlet boundary. The total turbulence kinetic energy is also calculated using the resolved velocity $\widetilde{u}_i(t)$ and the modelled turbulence kinetic energy $k_S(t)$.

To explain the proposed turbulent inflow generation method, the profiles of normalized longitudinal mean velocity and total turbulence kinetic energy with different averaging times at the inlet boundary are presented in Fig. 8a and Fig. 8b, respectively. The experimental results from the wind tunnel experiment by Ishihara et al. (1999) are used for validation. It is observed that the mean velocity and total turbulence kinetic energy do not change with the averaging time. Fig. 8c illustrates the variation in resolved and modelled turbulence kinetic energy with different averaging times. At the inlet boundary, the resolved turbulence kinetic energy decreases as the averaging time increases, while the modelled part increases, so the total turbulence kinetic energy does not change.

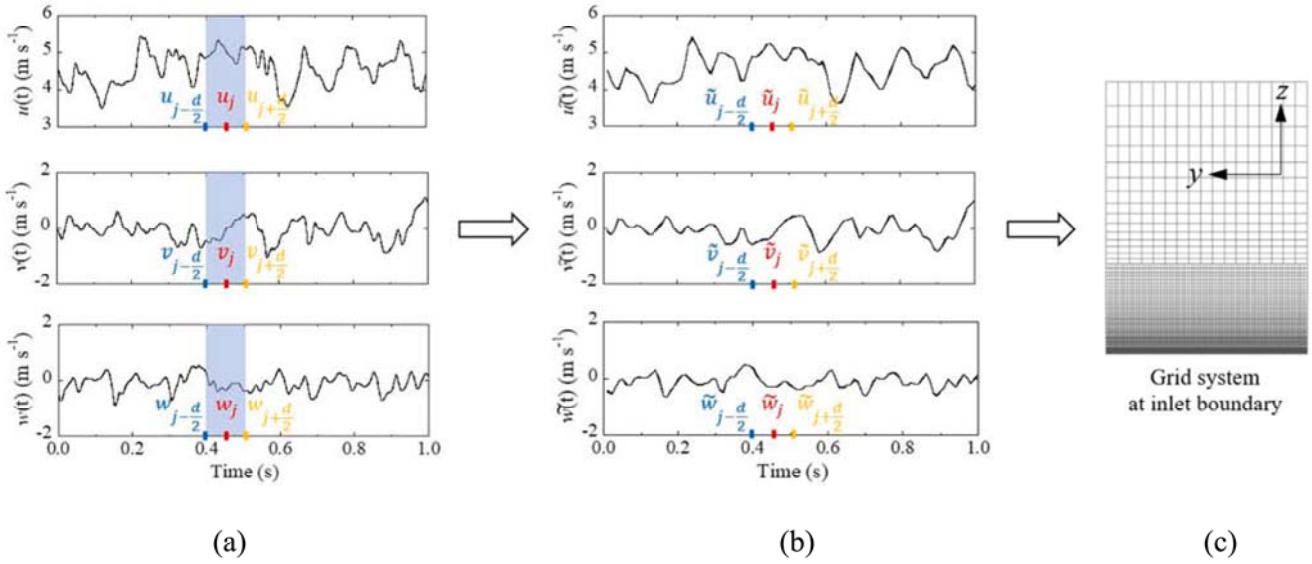

Fig. 7. The flowchart of the proposed turbulent inflow generation method; **a** Instantaneous velocity components; **b** Moving-averaged velocity components; **c** Inlet grid.

Table 1
Description of inflow data used in RANS, LES and URANS at the inlet boundary.

Turbulence model	Longitudinal velocity	Lateral velocity	Vertical velocity	Turbulence kinetic energy	Turbulence dissipation rate
RANS	$\overline{u}$	$\overline{v}$	$\overline{w}$	$\overline{k}$	$\overline{\varepsilon}$
LES	$u(t)$	$v(t)$	$w(t)$	—	—
URANS	$\widetilde{u}(t)$	$\widetilde{v}(t)$	$\widetilde{w}(t)$	$k_S(t)$	$\varepsilon_S(t)$

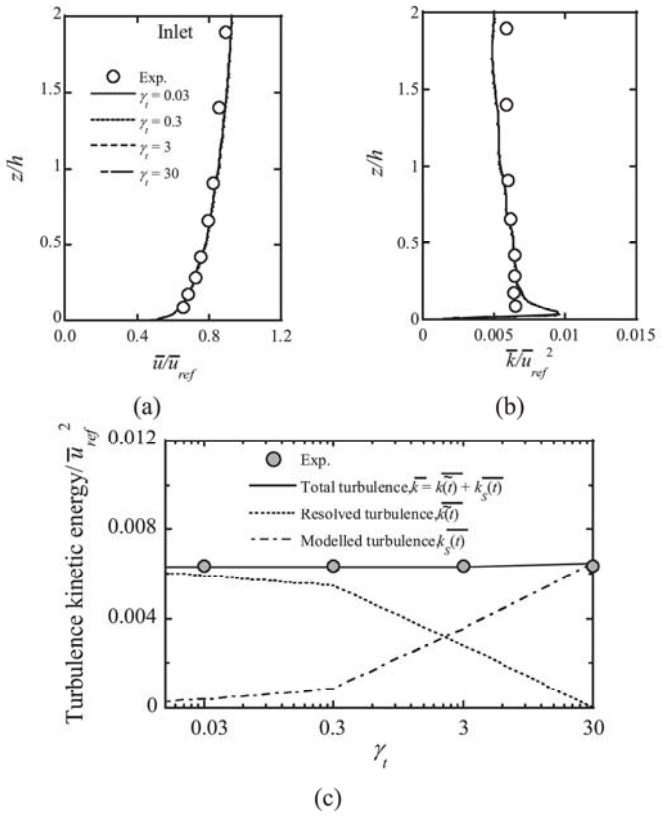

Fig. 8. Profiles of a normalized longitudinal mean velocity, b normalized total turbulence kinetic energy. c Variation of resolved and modelled turbulence kinetic energy with different averaging times, γ_t= 0.03, 0.3, 3 and 30 at the inlet boundary.

2.4. Indicators for evaluating performance of turbulence models

In this study, two indicators are used to evaluate prediction accuracy and computational efficiency of turbulence models. In terms of prediction accuracy, the hit rate is commonly employed to evaluate the consistency between numerical results and observed data (Schatzmann et al., 2010; Oettl, 2015; Ishihara and Qi, 2019), and is formulated as follows:

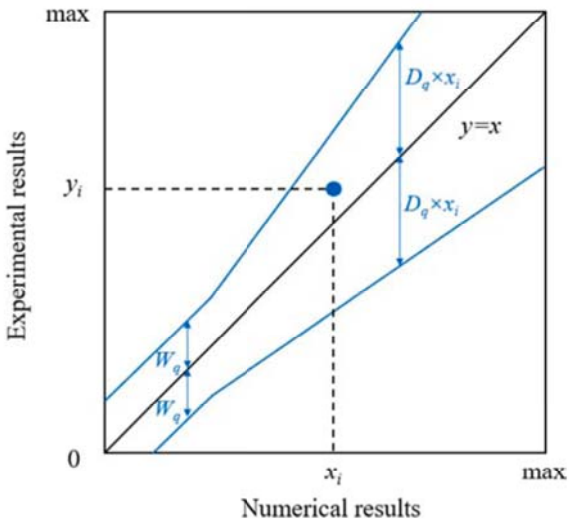

Fig. 9. Illustrations of validation metrics. Blue point is a datapoint; blue lines are thresholds.

$$q_j = \frac{1}{M}\sum_{i=1}^{M} m_i, with\, m_i = \begin{cases} 1, \left|\frac{y_i - x_i}{x_i}\right| \le D_q \text{or} |y_i - x_i| \le W_q \\ 0, \text{else} \end{cases} \quad (20)$$

where M is the total amount of data points. j can represents either the mean velocity U or the total turbulence kinetic energy K, i denotes the ith data. x_i are the experimental results for mean velocity and turbulence kinetic energy while y_i are the numerical results. The threshold D_q is 0.15 for the mean velocity while 0.3 for the turbulence kinetic energy, because a squared variable results in an error twice as large as the magnitude of the variable itself (Ishihara and Qi, 2019). $W_q = 0.05\,|max|$ is the same for the mean velocity and the turbulence kinetic energy, where $|max|$ represents the maximum of the numerical and experimental results. A hit rate of $q = 1$ indicates perfect prediction, meaning that all errors in the numerical results are within the threshold specified in Eq. (20). Conversely, if all errors in the numerical results exceed the threshold, then $q = 0$. The validation metrics according to Eq. (20) are illustrated in Fig. 9.

Regarding computational efficiency, Ferziger and Peric (2002) analyzed the efficiency of parallel programs using a speedup factor, which is described as the ratio of the computational time of serial algorithm with a single processor to that of the parallelized algorithm with n processors. Following this principle, in this study, the performance of computational efficiency is assessed by the ratio of computational time of turbulence models to that of RANS, as RANS is widely acknowledged for its excellent computational efficiency (Sidik et al., 2020), it is defined as follows:

$$e = \begin{cases} 0.1, T/T_{RANS} \in (32, +\infty) \\ 0.2, T/T_{RANS} \in (16, 32] \\ 0.4, T/T_{RANS} \in (8, 16] \\ 0.6, T/T_{RANS} \in (4, 8] \\ 0.8, T/T_{RANS} \in (2, 4] \\ 1.0, T/T_{RANS} \in (1, 2] \end{cases} \quad (21)$$

where T_{RANS} is the computational time of RANS and T is the computational time of other turbulence models. During RANS simulations, the residual values of six variables, i.e. mass, u, v, w, k and ε, are monitored and the solution is considered to have converged when these residual values are less than 10e-4. The computational time of RANS in this study is the time used to converge the numerical results. The cluster computing system used in this study is Intel Xeon CPU E5-2667 v4 with 88 cores and 960 GB memory.

A new indicator is proposed to assess both the prediction accuracy and computational efficiency of a turbulence model. The principle is that the higher the prediction accuracy as well as the computational efficiency, the better the turbulence model. The proposed indicator combines the accuracy and efficiency as follows:

$$S_j = q_j \times e^{\alpha} \quad (22)$$

where α ranges from 0 and 1. When α is zero, the proposed indicator depends on the hit rate and only the prediction accuracy is considered. In this study, an empirical value of $\alpha = 1/3$ is used, which can be appropriately selected according to the problem to balance the prediction accuracy and computational efficiency, and a satisfactory score for both accuracy and efficiency is defined as $S_j \ge 0.7$.

Another indicator to visualize the organized structures of a turbulent flow field is the quadrant analysis (Oikawa and Meng, 1995; Ishihara and Qi, 2019), which divides the product of velocity fluctuations u' and w' (also called momentum flux $-u'w'$) into four different quadrants shown as follows:

$$S_n(u'w') = \begin{cases} -\overline{u'w'}, \ for\ u' > 0 \ and\ w' > 0, n = 1; \\ -\overline{u'w'}, \ for\ u' < 0 \ and\ w' > 0, \ n = 2; \\ -\overline{u'w'}, for\ u' < 0 \ and\ w' < 0, n = 3; \\ -\overline{u'w'}, for\ u' > 0 \ and\ w' < 0, n = 4 \end{cases} \quad (23)$$

Quadrant two represents ejection events with fluctuating velocity components backward and upward. Sweep events are depicted in quadrant four with fluctuating velocity components forward and downward. Quadrants one and three stand for outward and wall ward interaction, with minimal contribution to the mean momentum flux (Poggi and Katul, 2007). The difference in momentum flux between sweep S_4 and ejection S_2, ΔS, is an indicator of the strength of organized motion. Specifically, a small ΔS represents the fully developed turbulent flow, while a large ΔS indicates the presence of organized motions, such as, large-scale vortex shedding and coherent structures.

3. Results and validation of URANS model

The turbulent fields over flat terrain, a line of trees and a steep hill predicted by URANS are investigated in Sections 3.2, 3.3 and 3.4, respectively.

3.1. Turbulent flow field over flat terrain

Fig. 10 shows the normalized longitudinal mean velocity and total turbulence kinetic energy over flat terrain reproduced by URANS with different averaging times at several downstream locations in the central plane. The profiles of mean velocity and total turbulence kinetic energy produced by URANS agree well with these by experiment. The averaging time used in URANS simulations for flat terrain is not sensitive since the turbulence over flat terrain is completely developed. Fig. 11 illustrates the variations of the resolved and modelled turbulence kinetic energy by URANS with different averaging times at the location P_3. The trends are similar to those observed at the inlet in Fig. 8c. This indicates that URANS can select large averaging times and save computational time with the same prediction accuracy for flat terrain.

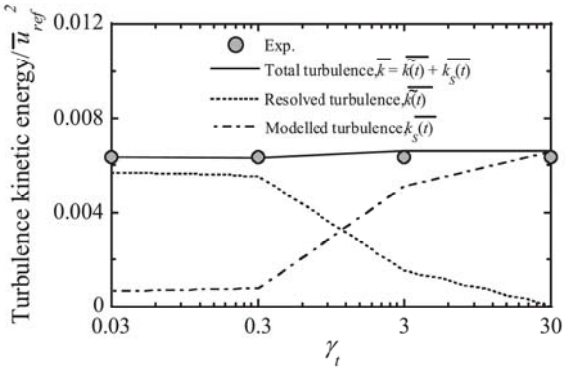

Fig. 11. Variation of resolved, modelled and total turbulence kinetic energy predicted by URANS at location P_3 with different averaging times.

3.2. Turbulent flow field around a line of trees

Fig. 12 presents the profiles of normalized longitudinal mean velocity and normalized total turbulence kinetic energy behind a line of trees predicted by URANS with different averaging times at several downstream locations in the central plane. The observation data in

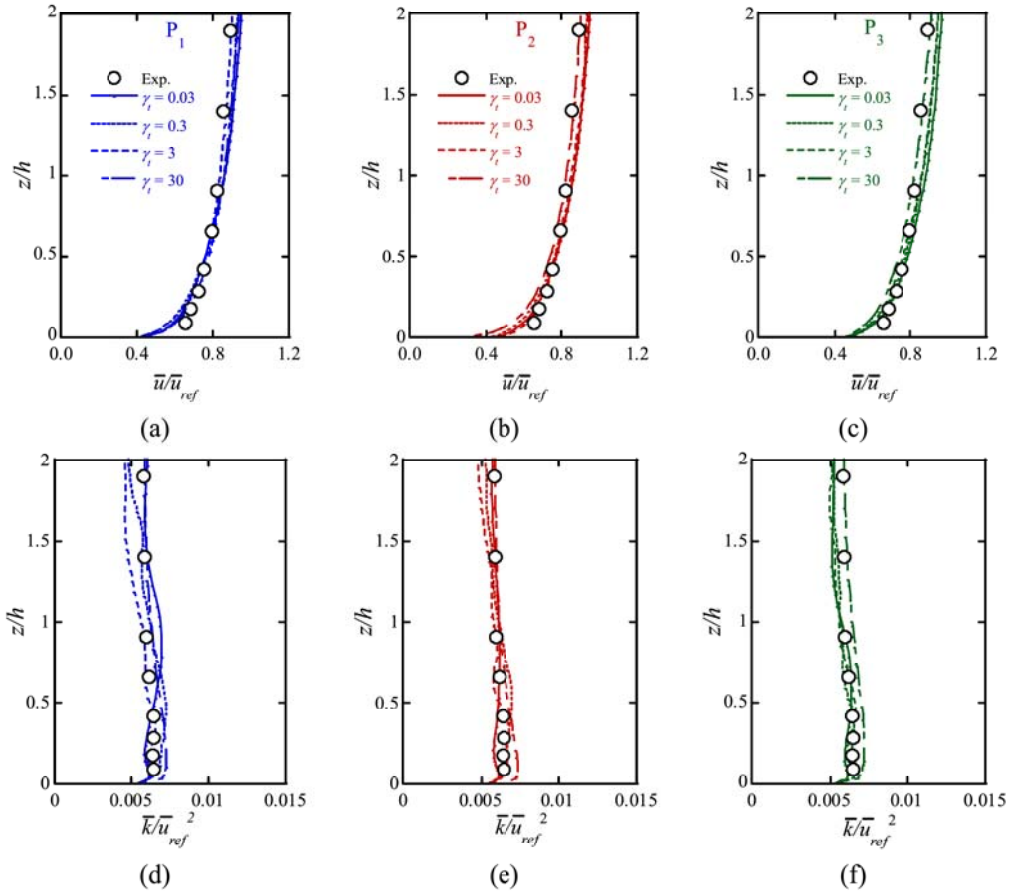

Fig. 10. Comparison of numerical and observed profiles of normalized longitudinal mean velocity at a P_1, b P_2, c P_3 and total turbulence kinetic energy at d P_1, e P_2, f P_3.

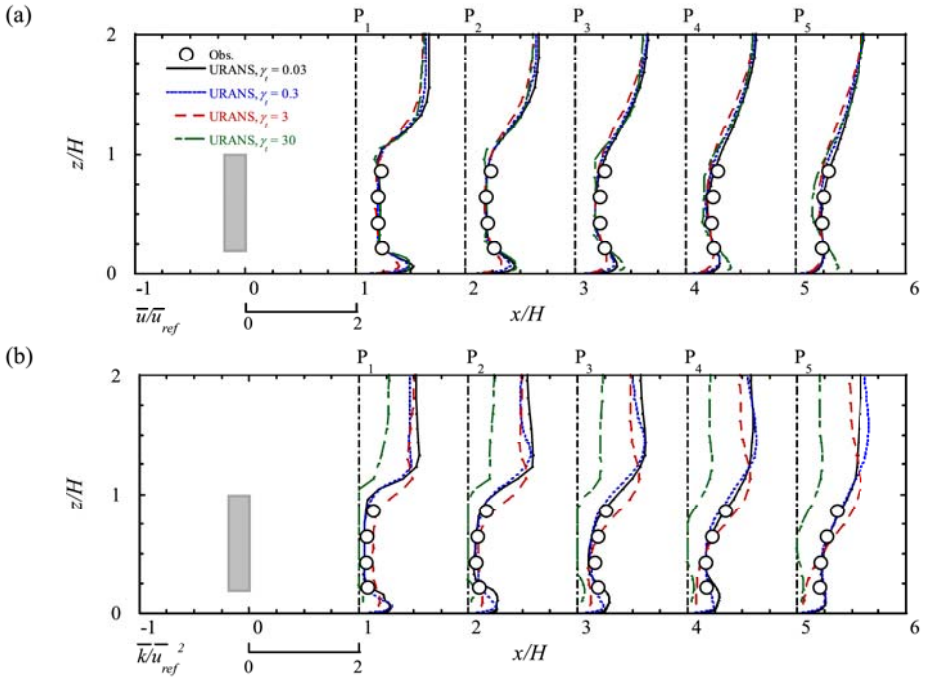

Fig. 12. Comparison of numerical and observed values: a normalized longitudinal mean velocity and b normalized total turbulence kinetic energy at several downstream locations behind the line of trees.

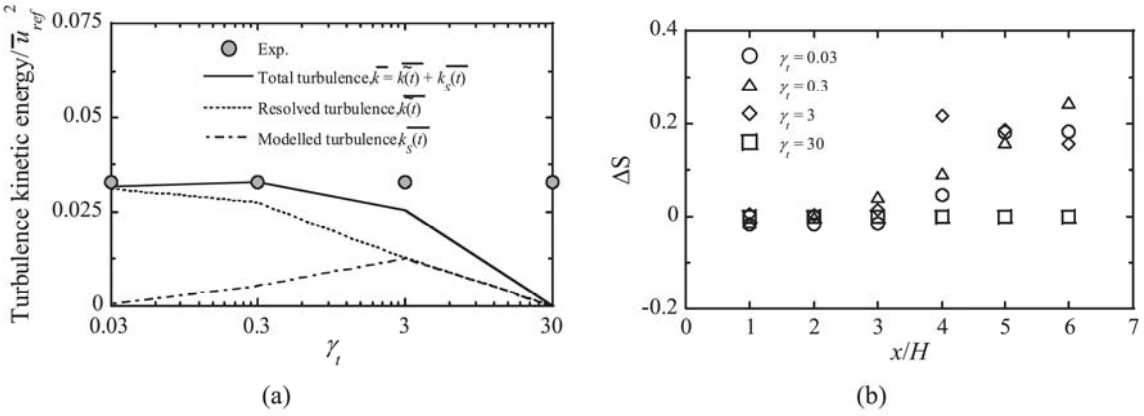

Fig. 13. A variation of resolved, modelled and total turbulence kinetic energy with averaging times at location $x/H = 4$, $y/H = 0$ and $z/H = 0.43$ and b variation of ΔS with distance downstream of the line of trees at height $z/H - 0.643$.

Fig. 12 are obtained from the field measurement by Kurotani et al (2001). It is obvious that URANS shows good agreement with the observed mean velocity when$\gamma_t \leq 3$, but significantly underestimates the observed turbulence kinetic energy when $\gamma_t = 30$.

To explain the contribution of the resolved and modelled turbulence kinetic energy to the total turbulence kinetic energy predicted by URANS with different averaging times, the variation of the resolved and modelled turbulence kinetic energy with averaging times is presented in Fig. 13a for $x/H = 4$, $y/H = 0$ and $z/H = 0.43$. As γ_t increases, the resolved turbulence kinetic energy decreases and the modelled part increases. However, for $\gamma_t \geq 3$, the modelled turbulence kinetic energy in wake does not increase sufficiently, resulting in a decrease of the total turbulence kinetic energy. The reason is that the low frequency motions behind the trees are filtered out by the long averaging time. This suggests that URANS needs an optimal averaging time to resolve the coherent structures downstream the line of trees. Fig. 13b illustrates the variation of ΔS with averaging times at several locations downstream of the trees at the height of $z/H = 0.643$. It clearly shows that the ΔS is nearly zero in the near wake region, while increases with downstream distance, indicating the presence of coherent structures behind the trees. However, ΔS is close to zero in every region when $\gamma_t = 30$, which means that the URANS with $\gamma_t = 30$ cannot capture the organized motions behind the trees.

To further investigate how the averaging time affect the coherent structures behind the trees, the vortex cores with $\lambda_2 = -2{,}000$ are visualized in Fig. 14. As the averaging time increases, the small vortices disappear, and the large vortices become less noticeable. For $\gamma_t \leq 3$, the URANS model provides an excellent flow description with visible coherent structures in wake of the trees. However, for $\gamma_t = 30$, URANS removes all low frequency motion, and the coherent structures completely disappear in wake region.

3.3. Turbulent flow field over a steep hill

Fig. 15 shows the profiles of normalized longitudinal mean velocity and normalized total turbulence kinetic energy over a steep hill

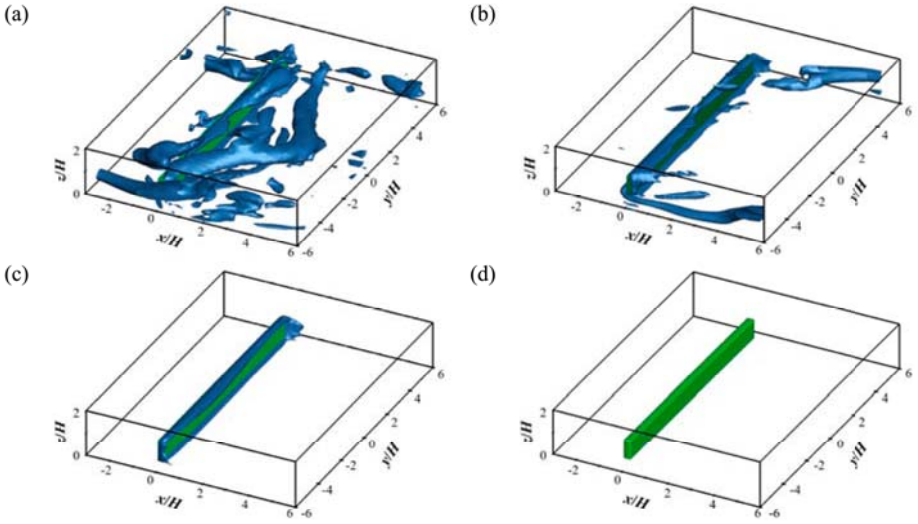

Fig. 14. Bird view of vortex cores around the row of trees with λ_2 = -2,000 predicted by URANS with a γ_t = 0.03, b γ_t = 0.3, c γ_t = 3 and d..γ_t = 30

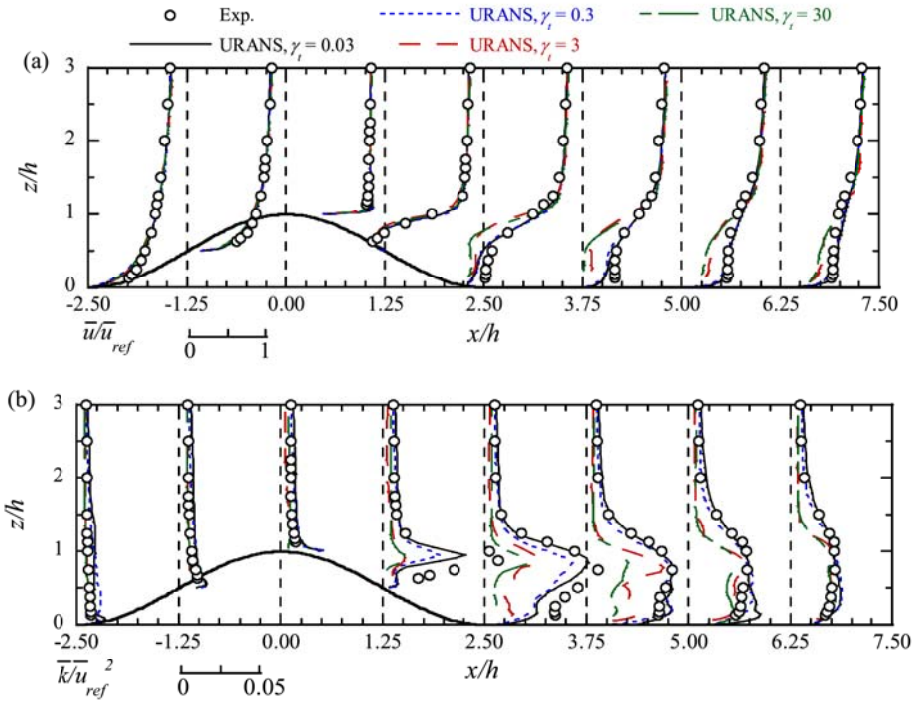

Fig. 15. Comparison of numerical and observed values: a normalized longitudinal mean velocity and b normalized total turbulence kinetic energy over a steep hill predicted by URANS with different averaging times.

predicted by URANS at $y/h = 0$ with different averaging times. It is found that for $\gamma_t \leq 0.3$, the predicted mean velocity by URANS is in satisfactory agreement with that by experiment. However, as γ_t increases, at the wake of the hill, the longitudinal mean velocity as well as total turbulence kinetic energy decrease within $z/h \leq 1.5$. Specifically, for $\gamma_t \geq 3$, the results predicted by URANS exhibit a large discrepancy with the experimental data.

Fig. 16a shows the variation of resolved, modelled and total turbulence kinetic energy predicted by URANS with different averaging times at location $x/h = 3.75$, $y/h = 0$ and $z/h = 0.5$. The resolved turbulence kinetic energy decreases with increase of the averaging time. Similar to the row of trees case, for $\gamma_t \geq 3$, the modelled turbulence kinetic energy in wake does not increase sufficiently, resulting in a decrease in the total turbulence kinetic energy. Fig. 16b presents the variation of ΔS with downstream distance around the steep hill at height $z'/h = 1$ above the ground surface predicted by URANS with different averaging times. For $\gamma_t = 30$, ΔS approaches zero, indicating that no coherent structures are reproduced, but for $\gamma_t \leq 3$, ΔS first increases and then decreases in the wake region, indicating the presence of organized motion caused by the horseshoe vortices behind the steep hill as show in Fig. 17, which displays the vortex cores around the steep hill with λ_2 = -7,000. As the averaging time increases, the small vortices disappear, and only the large vortices remain. The horseshoe vortices in the wake behind the steep hill are reproduced by URANS for $\gamma_t \leq 3$, while for $\gamma_t = 30$, there is no coherent structure behind the steep hill. This result explains why the conventional URANS cannot simulate the wake of steep hills in a turbulent boundary layer well when the mean velocity and total turbulence kinetic energy were used as the inlet boundary condition, as shown in Ishihara and Qi (2019), because when the mean velocity and total turbulence kinetic energy are imported to the inlet boundary, it means that

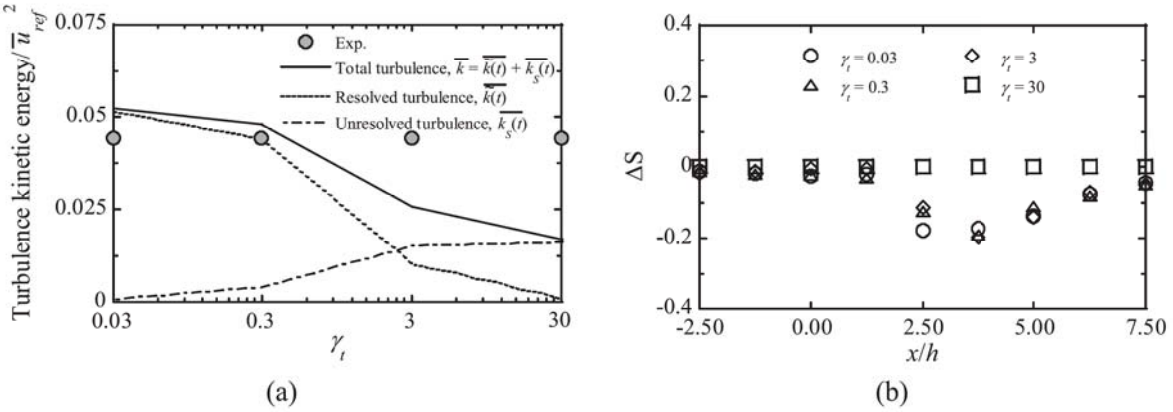

Fig. 16. **A** Variation of resolved, modelled and total turbulence kinetic energy with averaging time at location of $x/h = 3.75$, $y/h = 0$ and $z/h = 0.5$ and **b** variation of ΔS with distance downstream the steep hill at $z'/h = 1$ above the ground surface.

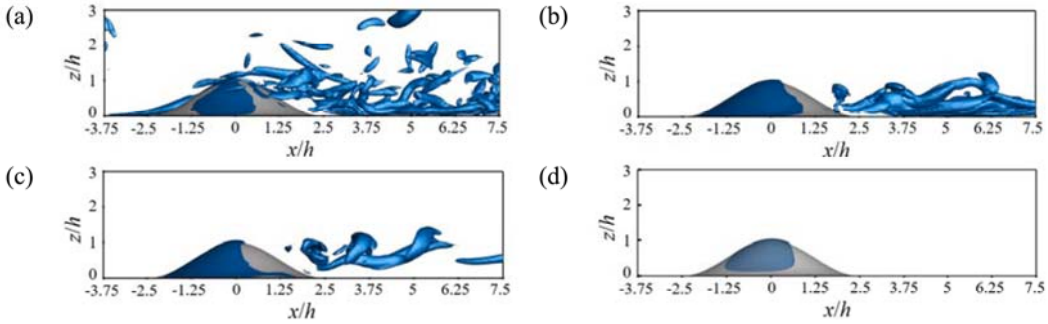

Fig. 17. Side view of vortex cores around the steep hill with $\lambda_2 = -7{,}000$ predicted by URANS with a $\gamma_t = 0.03$, b $\gamma_t = 0.3$, c $\gamma_t = 3$ and d..$\gamma_t = 30$

a very large averaging times is used.

4. Performance assessments of turbulence models

In Section 4.1, the performance of three turbulence models, namely, RANS, LES and URANS for predicting turbulent flows over flat terrain is evaluated, considering time and grid independence. The numerical results and performance evaluation of RANS, LES and URANS over a line of trees and a steep hill are then presented in Section 4.2 and 4.3.

4.1. Performance of turbulence models for flat terrain

To evaluate grid and time independence of RANS, LES and URANS, the profiles of normalized longitudinal mean velocity and total turbulence kinetic energy with respect to grid size and time step size are shown in Fig. 18 and Fig. 19, respectively. RANS shows good agreement even with a large grid size and long averaging time. LES is very sensitive to grid size and time step size and significantly underestimates total turbulence kinetic energy with large grid or long time step. Here, the grid size is expressed in real scale. Only with small grid size and short time step, LES provides good prediction accuracy. In contrast, URANS permits the use of larger grid sizes and longer time steps and s to meet the requirements of both prediction accuracy and computational efficiency because the conservation of total kinetic energy is satisfied during the simulation.

Table 2 summarizes the computational efficiency, hit rate and performance indicator of RANS, LES and URANS for predicting the turbulent flows over flat terrain. Since the database for turbulent inflow generation from LES can be reused, so the total computational time listed in Table 2 is just the running time for the computational domain shown in Fig. 3 and Fig. 5. Note that Table 2 shows the LES results with the same time step size used in Qi and Ishihara (2018). The cases with performance indicators larger than the threshold 0.7 are highlighted in red. For RANS, the performance indicators for mean velocity and total turbulence kinetic energy are larger than 0.7. LES shows the same prediction accuracy as URANS, but the computational time of LES is much longer than that of URANS. URANS generally provides better performance than LES for both mean velocity and turbulence kinetic energy. Although LES has good prediction accuracy, it takes a long computational time, and the performance indicators are lower than 0.7. The overall performance of URANS and RANS are better than that of LES for predicting flow fields without flow separation.

4.2. Performance of turbulence models for a line of trees

The profiles of normalized longitudinal mean velocity and total turbulence kinetic energy behind a line of trees predicted by RANS, LES and URANS with different γ_t are presented in Fig. 20, where the grid size of three turbulent models is the same and the time step size in the LES simulation is constant as used in Qi and Ishihara (2018). RANS demonstrates favorable agreement in predicting mean velocity but significantly underestimates turbulence kinetic energy because the vortices in the energy containing range are not reproduced, as pointed out by Qi and Ishihara (2018). LES performs well with small time step. URANS

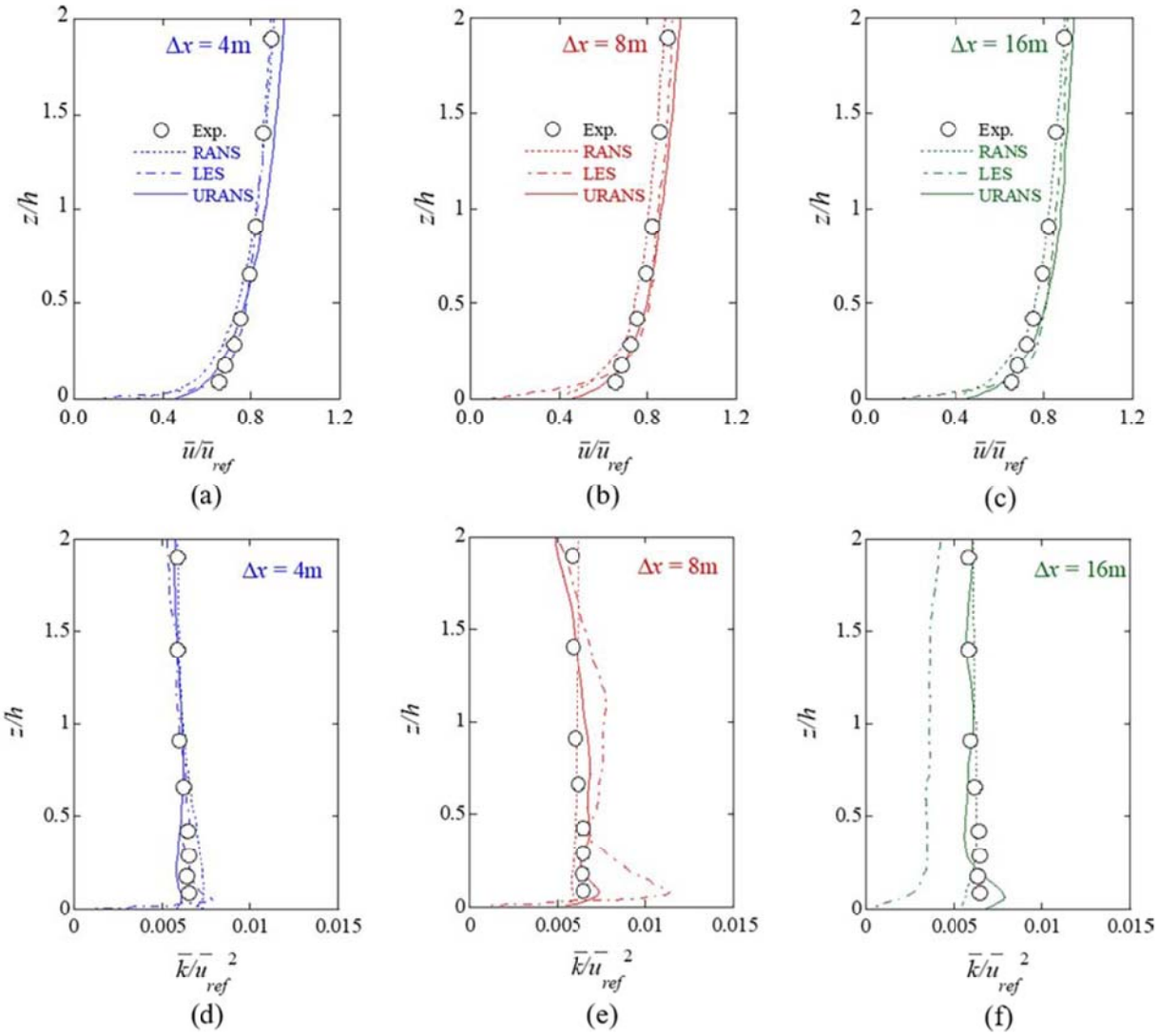

Fig. 18. Profiles of normalized longitudinal mean velocity and total turbulence kinetic energy over flat terrain predicted by RANS, LES and URANS with different grid sizes and $\gamma_t = 0.03$: a, d $\Delta x = 4$ m, b, e $\Delta x = 8$ m, c, f $\Delta x = 16$ m at P_2 in Fig. 5.

predicts the mean and turbulent flow fields with sufficient accuracy for all averaging times. This means that $\gamma_t = 3$ is the best averaging time for URANS to predict the turbulent flow behind a line of trees because it captures vortices in the energy containing range as shown in Fig. 2.

A summary of computational efficiency, hit rate and performance indicator of RANS, LES and URANS for predicting the turbulent flows around the row of trees is presented in Table 3. RANS has poor prediction accuracy of the mean velocity and significantly underestimates turbulence kinetic energy, resulting in poor performance indicators. LES shows favorable prediction accuracy of the mean velocity and turbulence kinetic energy but the computational time is quite long. URANS shows favorable prediction accuracy for both the mean velocity and total turbulence kinetic energy even for longer averaging times ($\gamma_t = 3$). The performance indicators of URANS are higher than those of RANS and LES because URANS provides better prediction accuracy and computational efficiency for a line of trees.

4.3. Performance of turbulence models for a steep hill

Fig. 21 shows the profiles of normalized longitudinal mean velocity and total turbulence kinetic energy at $x/h = 3.75$ and $y/h = 0$ predicted by RANS, LES and URANS with $\gamma_t = 0.03$, 0.3 and 3, where the grid size of three turbulent models is the same and the time step size in the LES simulation is constant as used in Qi and Ishihara (2018). RANS significantly underestimates both the longitudinal mean velocity and total turbulence kinetic energy, as indicated by Ishihara and Qi (2019). LES shows good agreement with experimental results with small time step. In contrast, URANS shows favorable agreement for both the longitudinal mean velocity and total turbulence kinetic energy when $\gamma_t \leq 0.3$, while underestimates those when $\gamma_t = 3$, due to its inability to fully capture the

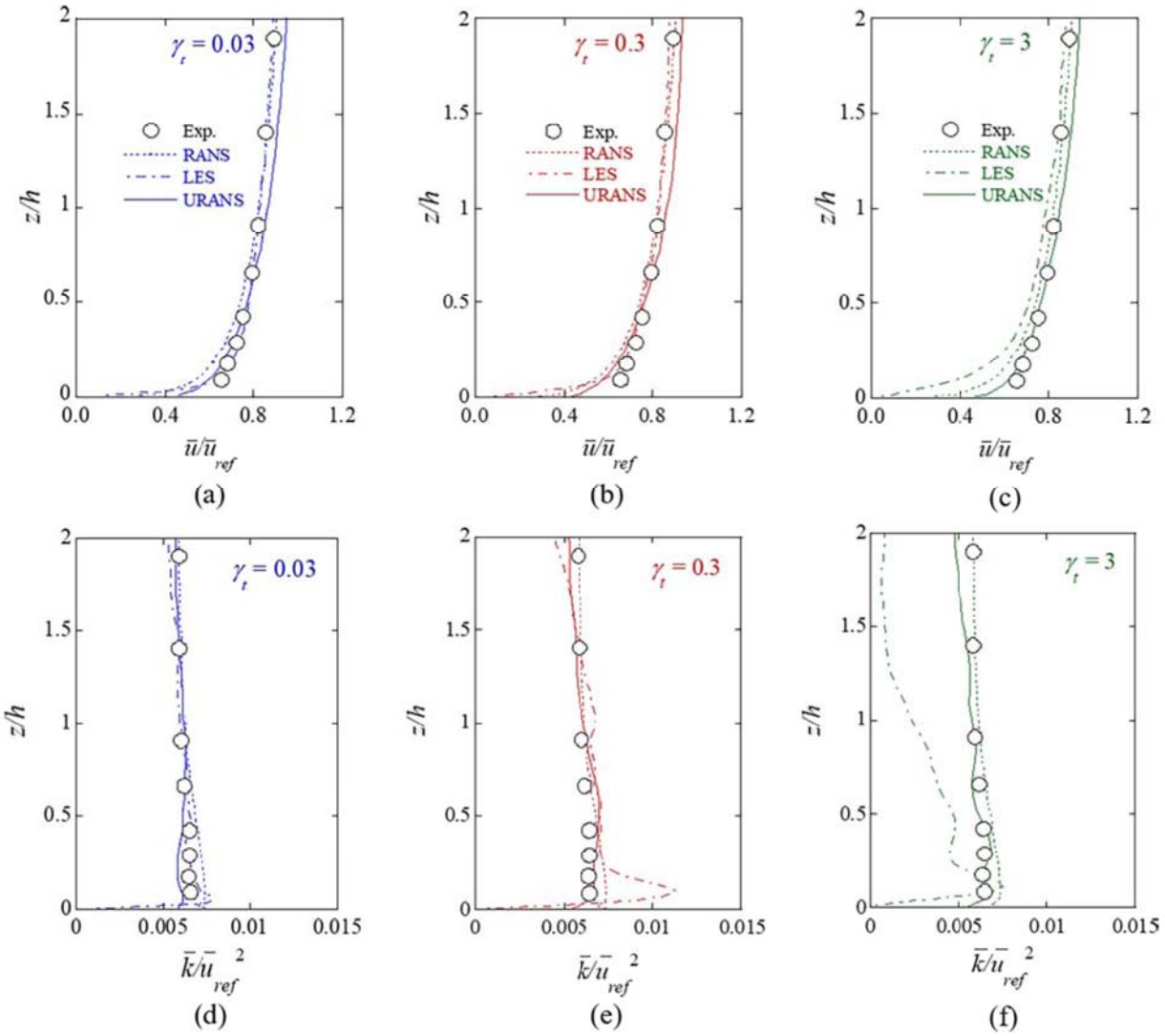

Fig. 19. Profiles of normalized longitudinal mean velocity and total turbulence kinetic energy over flat terrain predicted by SRANS, LES and URANS with different averaging times and Δx = 4 m: a, d $\gamma_t = 0.03$, b, e $\gamma_t = 0.3$, c, f $\gamma_t = 3$ at P_2 in Fig. 5.

Table 2
Summary of computational efficiency e, hit rate q_j, and performance indicator S_j of RANS, LES and URANS for predicting the turbulent flows over flat terrain based on the data below z/h = 2 as shown in Fig. 19.

Turbulence model	Averaging time	Computation time	e	q_j		S_j (α = 1/3)	
				q_U	q_K	S_U	S_K
RANS	—	0.35	1.00	0.88	1.00	0.88	1.00
LES	—	31.23	0.10	1.00	1.00	0.46	0.46
URANS	$\gamma_t = 0.03$	9.29	0.20	1.00	1.00	0.58	0.58
	$\gamma_t = 0.3$	2.75	0.60	1.00	1.00	0.84	0.84
	$\gamma_t = 3$	0.40	1.00	1.00	1.00	1.00	1.00

coherent structures in wake of the steep hill.

Table 4 summarizes the computational efficiency, hit rate and performance indicator of RANS, LES and URANS for predicting the turbulent flows over the steep hill. RANS has low prediction accuracy, resulting in low performance indicators of mean velocity and total turbulence kinetic energy in wake of a steep hill. LES has good prediction accuracy of the mean velocity and total turbulence kinetic energy but long computational time. Meanwhile, URANS provides acceptable

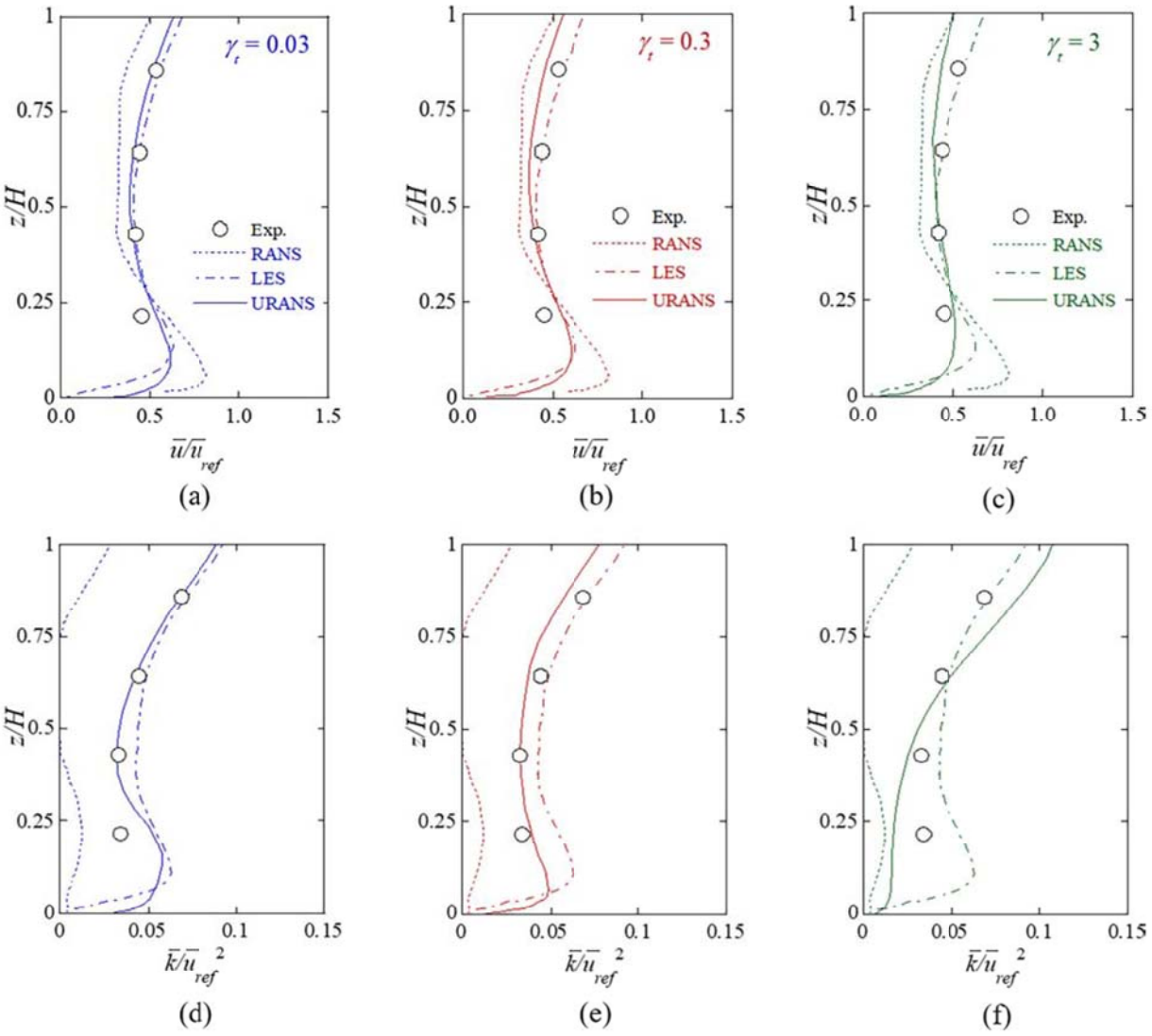

Fig. 20. Profiles of normalized longitudinal wind velocity around a line of trees at $x/H = 4$ and $y/H = 0$ predicted by RANS, LES and URANS with a $\gamma_t = 0.03$, b $\gamma_t = 0.3$, c $\gamma_t = 3$; Profiles of normalized total turbulence kinetic energy predicted by RANS, LES and URANS with d $\gamma_t = 0.03$, e $\gamma_t = 0.3$, f..$\gamma_t = 3$

Table 3
Summary of computational efficiency e, hit rate q_j and performance indicator S_j of RANS, LES and URANS for predicting the turbulent flows around a line of trees in the wake regions from $x/H = 1$ to $x/H = 5$ as shown in Fig. 12.

Turbulence model	Averaging time	Computation time	e	q_j		S_j ($\alpha = 1/3$)	
				q_U	q_K	S_U	S_K
RANS	—	0.20	1.00	0.55	0.00	0.55	0.00
LES	—	10.38	0.10	1.00	0.80	0.46	0.37
URANS	$\gamma_t = 0.03$	2.63	0.20	1.00	0.95	0.74	0.70
	$\gamma_t = 0.3$	0.87	0.60	0.85	0.85	0.71	0.71
	$\gamma_t = 3$	0.23	1.00	0.80	0.75	0.80	0.75

prediction accuracy and computational efficiency, thus, URANS meets the requirement of both performance indicators. When $\gamma_t = 3$, URANS has low performance indicator of the total turbulent kinetic energy. This means that $\gamma_t = 0.3$ is the optimal averaging time for URANS to predict turbulent flows in wake of a steep hill because the vortex shedding is well captured as illustrated in Fig. 17b.

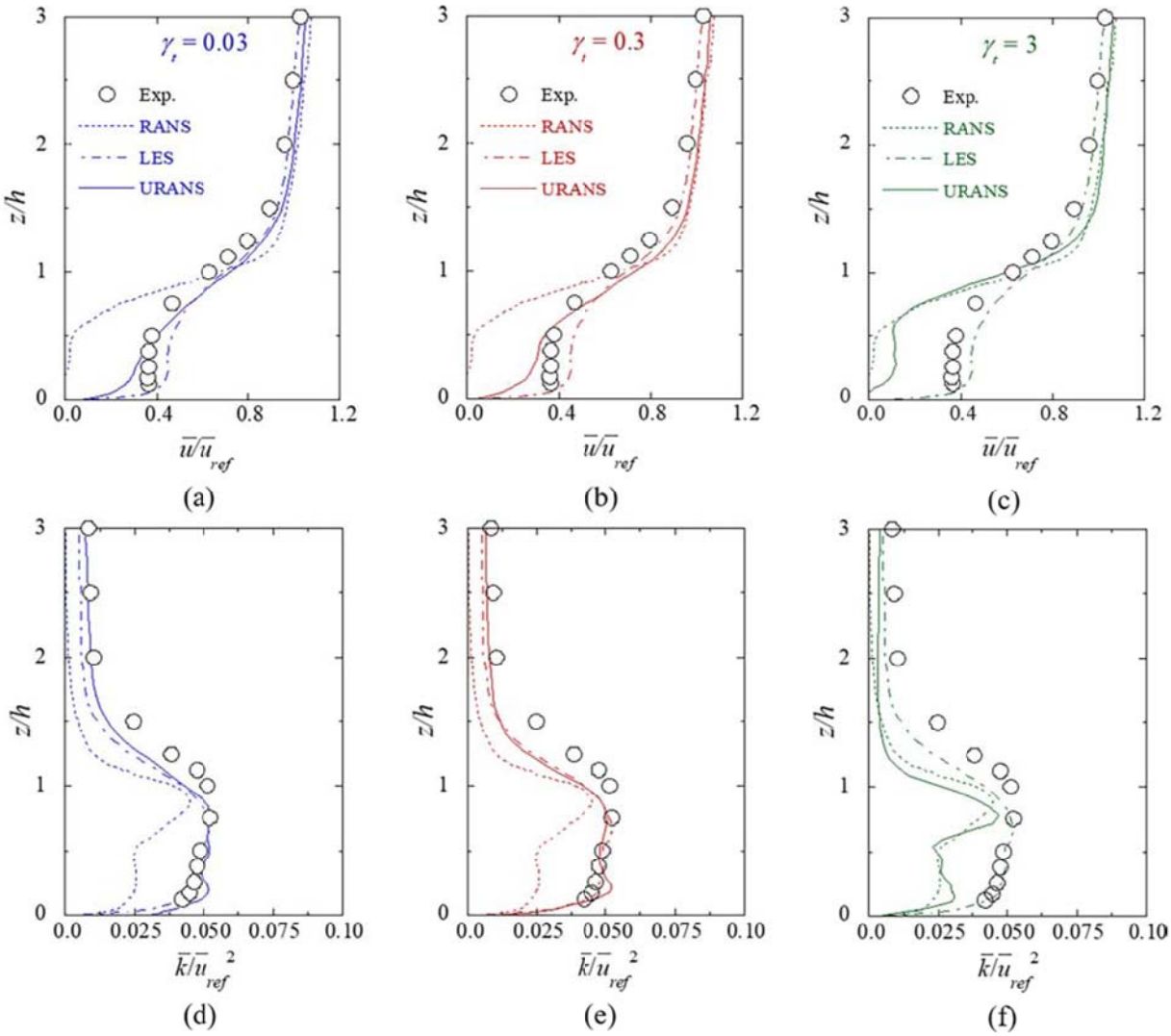

Fig. 21. Profiles of normalized longitudinal mean velocity over a steep hill by RANS, LES and URANS with a $\gamma_t = 0.03$, b $\gamma_t = 0.3$, c $\gamma_t = 3$. Profiles of normalized total turbulence kinetic energy at the same location predicted by RANS, LES and URANS with d $\gamma_t = 0.03$, e $\gamma_t = 0.3$, f..$\gamma_t = 3$

Table 4
Summary of computational efficiency e, hit rate $\boldsymbol{q}_j$ and performance indicator $\boldsymbol{S}_j$ of RANS, LES and URANS for predicting the turbulent flow fields over a steep hill in the wake region from x/h = 1.25 to x/h = 6.25 as shown in Fig. 15.

Turbulence model	Averaging time	Computation time	e	q_j		S_j (α = 1/3)	
				q_U	q_K	S_U	S_K
RANS	—	0.35	1.00	0.68	0.30	0.68	0.30
LES	—	31.16	0.10	0.91	0.97	0.42	0.45
URANS	$\gamma_t = 0.03$	9.32	0.20	0.89	0.82	0.52	0.48
	$\gamma_t = 0.3$	2.76	0.60	0.86	0.89	0.72	0.75
	$\gamma_t = 3$	0.41	1.00	0.76	0.43	0.76	0.43

5. Conclusions

In this study, a turbulent inflow generation method is proposed for the unsteady Reynolds-Averaged Navier-Stokes (URANS) model. Turbulent flow fields reproduced by URANS using the generated turbulent inflows are then validated by comparing with these by experiments. The performance of RANS, LES and URANS models is also evaluated by the proposed indicators. The following conclusions are obtained,

1. A new turbulent inflow generation method for URANS is proposed by defining a prespecified averaging time to determine the window width of the low-pass filter. The proposed inflow generation method is used to separate the turbulent inflow into a resolved part and a modelled part. The former is directly resolved by the URANS simulation, and the latter is predicted by the turbulence model. As the averaging time increases, the resolved turbulence kinetic energy decreases and the modelled component increases, while the conservation of total turbulence kinetic energy is satisfied during the simulation.
2. The mean velocity and total turbulence kinetic energy predicted by URANS over flat terrain, a line of trees and a steep hill are validated using the experimental data to clarify the effect of averaging time. Large averaging times can be applied to URANS over flat terrain and a line of trees, but a suitable averaging time is required for URANS to predict the large vortex shedding behind the steep hill as resolved coherent structures. The advantage of URANS is that it can predict the coherent structures as resolved vortices and the random motions as the modelled turbulence kinetic energy.
3. The performance of RANS, LES and URANS is evaluated by the proposed indicators using three turbulent flow fields. LES scores higher than RANS due to its better prediction accuracy on a line of trees, while RANS scores higher than LES due to its shorter computational time over flat terrain. URANS using turbulent inflows exhibits the overall best performance in predicting the mean velocity and turbulence kinetic energy compared to RANS and LES.

CRediT authorship contribution statement

Takeshi Ishihara: Writing – review & editing, Supervision, Resources, Methodology, Funding acquisition, Conceptualization. **Xiangyan Chen:** Writing – original draft, Visualization, Software, Investigation, Formal analysis, Data curation.

Declaration of competing interest

The authors declare that they have no known competing financial interests or personal relationships that could have appeared to influence the work reported in this paper.

Acknowledgement

This research is carried out as part of a joint program for next generation energy infrastructure with Toshiba Energy Systems & Solutions Corporation, J-POWER, Shimizu Corporation, Class NK, Tokyo Gas, CHOBU Electric Power. The authors express their deepest gratitude to the concerned parties for their assistance during this study. The authors also wish to thank the China Scholarship Council (Grant No. CSC202006130016) for the funding support.

Data availability

Data will be made available on request.

References

Baglietto, E., Lenci, G., Concu, D., 2017. STRUCT: A second-generation USRANS approach for effective design of advanced systems. In: Proceedings of the ASME 2017 Fluids Engineering Division Summer Meeting, Hawaii, USA p. V01BT12A004. http://dx.doi.org/10.1115/FEDSM2017-69241.

Balogh, M., Parente, A., Benocci, C., 2012. RANS simulation of ABL flow over complex terrains applying an enhanced k-ε model and wall function formulation: implementation and comparison for fluent and OpenFOAM. J. Wind Eng. Ind. Aerodyn. 104–106 (2012), 360–368. https://doi.org/10.1016/j.jweia.2012.02.023.

Blocken, B., Carmeliet, J., 2006. On the accuracy of wind-driven rain measurements on buildings. Build. Environ. 41 (12), 1798–1810. https://doi.org/10.1016/j.buildenv.2005.07.022.

Blocken, B., Carmeliet, J., 2008. Pedestrian wind conditions at outdoor platforms in a high-rise apartment building: generic sub-configuration validation, wind comfort assessment and uncertainty issues. Wind Struct. 11 (1), 51–70. https://doi.org/10.12989/was.2008.11.1.051.

Blocken, B., Deszö, G., Beeck, J.V., Carmeliet, J., 2010. Comparison of calculation models for wind-driven rain deposition on building facades. Atmos. Environ. 44 (14), 1714–1725. https://doi.org/10.1016/j.atmosenv.2010.02.011.

Chen, X., Liu, Z., Wang, X., Chen, Z., Xiao, H., Zhou, J., 2020. Experimental and numerical investigation of wind characteristics over mountainous valley bridge site considering improved boundary transition sections. Appl. Sci. 10 (3), 1–23. https://doi.org/10.3390/app10030751.

Feng, J., Xu, L., Baglietto, E., 2021. Assessing the applicability of the structure-based turbulence resolution approach to nuclear safety-related issues. Fluids 6 (61), 1–14. https://doi.org/10.3390/fluids6020061.

Ferreira, A.D., Lopes, A., Viegas, D.X., Sousa, A., 1995. Experimental and numerical simulation of flow around two-dimensional hills. J. Wind Eng. Ind. Aerodyn. 54 (94), 173–181. https://doi.org/10.1016/0167-6105(94)00040-K.

Ferziger, J., Peric, M., 2002. Computational method for fluid dynamics, 3rd edn. Springer, Berlin.

Fluent, 2021. Ansys Fluent Theory Guide. Ansys Inc. https://dl.cfdexperts.net/cfd_resources/Ansys_Documentation/Fluent/Ansys_Fluent_Theory_Guide.pdf.

Girimaji, S.S., 2006. Partially-averaged Navier-Stokes model for turbulence: a Reynolds-averaged Navier-Stokes to direct numerical simulation bridging method. J. Appl. Mech. 73 (3), 413–421. https://doi.org/10.1115/1.2151207.

Hart, J., 2016. Comparison of turbulence modeling approaches to the simulation of a dimpled sphere. Procedia. Eng. 147, 68–73.

Hooff, T.V., Blocken, B., 2013. CFD evaluation of natural ventilation of indoor environments by the concentration decay method: CO_2 gas dispersion from a semi-enclosed stadium. Build. Environ. 61 (2013), 1–17. https://doi.org/10.1016/j.buildenv.2012.11.021.

Iizuka, S., Kondo, H., 2004. Performance of various sub-grid scale models in large-eddy simulations of turbulent flow over complex terrain. Atmos. Environ. 38 (2004), 7083–7091. https://doi.org/10.1016/j.atmosenv.2003.12.050.

Ishihara, T., Hibi, K., Oikawa, S., 1999. A wind tunnel study of turbulent flow over a three-dimensional steep hill. J. Wind Eng. Ind. Aerodyn. 83, 95–107. https://doi.org/10.1016/S0167-6105(99)00064-1.

Ishihara, T., Hibi, K., 2002. Numerical study of turbulent wake flow behind a three-dimensional steep hill. Wind Struct. 5 (2–4), 317–328. https://doi.org/10.12989/was.2002.5.2_4.317.

Ishihara, T., Qi, Y., 2019. Numerical study of turbulent flow fields over steep terrain by using modified delayed detached-eddy simulations. Boundary-Layer Meteorol. 170 (1), 45–68. https://doi.org/10.1007/s10546-018-0389-8.

Ishihara, T., Qian, G., Qi, Y., 2020. Numerical study of turbulent flow fields in urban areas using modified k-ε model and large eddy simulation. J. Wind Eng. Ind. Aerodyn. 206 (2020), 1–20. https://doi.org/10.1016/j.jweia.2020.104333.

Janssen, W.D., Blocken, B., Hooff, T.V., 2013. Pedestrian wind comfort around buildings: comparison of wind comfort criteria based on whole-flow field data for a complex case study. Build. Environ. 59, 547–562. https://doi.org/10.1016/j.buildenv.2012.10.012.

Karava, P., Stathopoulos, T., 2012. Wind-induced internal pressures in buildings with large façade openings. J. Eng. Mech. 138 (4), 358–370. https://doi.org/10.1061/(ASCE)EM.1943-7889.0000296.

Kato, M., Launder, B.E., 1993. The modeling of turbulent flow around stationary and vibrating square cylinders. Ninth Symposium on turbulent Shear Flows, pp.10-4, Kyoto, Japan.

Keating, A., Piomelli, U., Balaras, E., Kaltenbach, H.J., 2004. A priori and a posteriori tests of inflow conditions for large-eddy simulation. Phys. Fluids. 16 (12), 4696–4712. https://doi.org/10.1063/1.1811672.

Kobayashi, T., Sagara, K., Yamanaka, T., Kotani, H., Takeda, S., Sandberg, M., 2009. Stream tube based analysis of problems in prediction of cross-ventilation rate. Int. J. Vent. 7, 321–334. https://doi.org/10.1080/14733315.2009.11683822.

Kubilay, A., Derome, D., Blocken, B., Carmeliet, J., 2013. CFD simulation and validation of wind-driven rain on a building facade with an Eulerian multi-phase model. Build. Environ. 61, 69–81. https://doi.org/10.1016/j.buildenv.2012.12.005.

Kurotani, Y., Kiyota, N., Kobayashi, S., 2001. Windbreak effect of tsuijimatsu in Izumo: Part 2. In: In: Proceedings of Architectural Institute of Japan, pp. 745–746.

Lenci, G., 2016. A methodology based on local resolution of turbulent structures for effective modeling of unsteady flows. Massachusetts Institute of Technology, Massachusetts, USA. Dissertation.

Luis, T.W.C., 2012. Numerical Simulation of the Dynamics of Turbulent Swirling Flames. Technische Universität München, Munich, GER. Dissertation.

Mikuz, B., Tiselj, I., 2017. URANS prediction of flow fluctuations in rod bundle with split-type spacer grid. Int. J. Heat Fluid Fl. 64, 10–22. https://doi.org/10.1016/j.ijheatfluidflow.2017.01.008.

Munters, W., Meneveau, C., Meyers, J., 2016. Turbulent inflow precursor method with time-varying direction for large-eddy simulations and applications to wind farms. Boundary-Layer Meteorol. 159 (2), 305–328. https://doi.org/10.1007/s10546-016-0127-z.

Oettl, D., 2015. Quality assurance of the prognostic, microscale wind-field modelGRAL14.8 using wind-tunnel data provided by the German VDI guideline 3783-9. J. Wind Eng. Ind. Aerodyn. 142 (2015), 104–110. https://doi.org/10.1016/j.jweia.2015.03.014.

Oikawa, S., Meng, Y., 1995. Turbulence characteristics and organized motion in a suburban roughness sublayer. Boundary-Layer Meteorol. 74 (3), 289–312.

Oka, S., Ishihara, T., 2009. Numerical study of aerodynamic characteristics of a square prism in a uniform flow. J. Wind Eng. Ind. Aerodyn. 97 (11), 548–559. https://doi.org/10.1016/j.jweia.2009.08.006.

Poggi, D., Katul, G., 2007. The ejection-sweep cycle over bare and forested gentle hills: a laboratory experiment. Boundary-Layer Meteorol. 122, 493–515. https://doi.org/10.1007/s10546-006-9117-x.

Qi, Y., Ishihara, T., 2018. Numerical study of turbulent flow fields around of a row of trees and an isolated building by using modified k-ε model and LES model. J. Wind Eng. Ind. Aerodyn. 177 (2018), 293–305. https://doi.org/10.1016/j.jweia.2018.04.007.

Qian, G., Ishihara, T., 2019. Numerical study of wind turbine wakes over escarpments by a modified delayed detached eddy simulation. J. Wind Eng. Ind. Aerodyn. 191 (2019), 41–53. https://doi.org/10.1016/j.jweia.2019.05.004.

Ren, H., Laima, S., Chen, W., Zhang, B., Guo, A., Li, H., 2018. Numerical simulation and prediction of spatial wind field under complex terrain. J. Wind Eng. Ind. Aerodyn. 180 (2018), 49–65. https://doi.org/10.1016/j.jweia.2018.07.012.

Rodi, W., 1993. On the simulation of turbulent flow past bluff bodies. J. Wind Eng. Ind. Aerodyn. 69–71, 55–75. https://doi.org/10.1016/B978-0-444-81688-7.50005-X.

Schatzmann, M., Olesen, H., Franke, J., 2010. COST 732 model evaluation case studies: approach and results. COST Office Brussels, 121 pp.

Shimada, K., Ishihara, T., 2002. Application of a modified k-ε model to the prediction of aerodynamic characteristics of rectangular cross-section cylinders. J. of Fluid and Struct. 16 (4), 465–485. https://doi.org/10.1006/jfls.2001.0433.

Sidik, N.A.C., Yusuf, S.N.A., Asako, Y., Mohamed, S.B., Japa, W.M.A.A., 2020. A short review on rans turbulence models. CFD Letters 12 (11), 83–96. https://doi.org/10.37934/cfdl.12.11.8396.

Spalart, P.R., 2000. Strategies for turbulence modelling and simulations. Int. J. of Heat Fluid Fl. 21, 252–263. https://doi.org/10.1016/S0142-727X(00)00007-2.

Tominaga, Y., 2015. Flow around a high-rise building using steady and unsteady SRANS CFD: effect of large-scale fluctuations on the velocity statistics. J. Wind Eng. Ind. Aerodyn. 142 (2015), 93–103. https://doi.org/10.1016/j.jweia.2015.03.013.

Tsang, C.W., Kwok, K.C.S., Hitchcock, P.A., 2012. Wind tunnel study of pedestrian level wind environment around tall buildings: effects of building dimensions, separation and podium. Build. Environ. 49 (2012), 167–181. https://doi.org/10.1016/j.buildenv.2011.08.014.

Wang, Z., Zhang, Z., Wu, C., 2022. Numerical investigation on the nonlinear flutter behaviors of a π-shaped sectional bridge deck. Adv. Struct. Eng. 25 (10), 2157–2174. https://doi.org/10.1177/13694332221090291.

Watanabe, F., Uchida, T., 2015. Micro-siting of wind turbine in complex terrain: simplified fatigue life prediction of main bearing in direct drive wind turbines. Wind Eng. 39 (4), 349–368. https://doi.org/10.1260/0309-524X.39.4.349.

Xu, L., 2020. Second generation Unsteady Reynolds Averaged Navier Stokes approach for application to aerodynamic design and optimization in the automotive industry. Massachusetts Institute of Technology, Massachusetts, USA. Dissertation.

Yakhot, V., Orszag, S.A., Thangam, S., Gatski, T.B., Speziale, C.G., 1992. Development of turbulence models for shear flows by a double expansion technique. Physics of Fluids A 4, 1510–1520. https://doi.org/10.1063/1.858424.

Yamaguchi, A., Ishihara, T., Fujino, Y., 2003. Experimental study of the wind flow in a coastal region of Japan. J. Wind Eng. Ind. Aerodyn. 91 (2003), 247–264. https://doi.org/10.1016/S0167-6105(02)00349-5.

Yang, Z., 2015. Large-eddy simulation: Past, present and the future. Chinese J. Aeronaut. 28 (1), 11–24. https://doi.org/10.1016/j.cja.2014.12.007.

Yang, Q., Zhou, T., Yan, B., Pham, V.P., Hu, W., 2020. LES study of turbulent flow fields over hilly terrains - Comparisons of inflow turbulence generation methods and SGS models. J. Wind Eng. Ind. Aerodyn. 204, 1–23. https://doi.org/10.1016/j.jweia.2020.104230.

Yang, Q., Zhou, T., Yan, B., Liu, M., Pham, V.P., Shu, Z., 2021. LES study of topographical effects of simplified 3D hills with different slopes on ABL flows considering terrain exposure conditions. J. Wind Eng. Ind. Aerodyn. 210 (2021), 1–13. https://doi.org/10.1016/j.jweia.2020.104513.

Younis, B.A., Przulj, V.P., 2006. Computation of turbulent vortex shedding. Comput. Mech. 37, 408–425.

Zhang, R., Liu, Z., Wang, L., Chen, Z., 2021. A practical method for predicting post-flutter behavior of a rectangular section. J. Wind Eng. Ind. Aerodyn. 216, 1–10. https://doi.org/10.1016/j.jweia.2021.104707.

Zhou, T., Yang, Q., Yan, B., Deng, X., Yuan, Y., 2022. Detached eddy simulation of turbulent flow fields over steep hilly terrain. J. Wind Eng. Ind. Aerodyn. 221, 1–14. https://doi.org/10.1016/j.jweia.2022.104906.